

## The Kinematics, Orbit, and Survival of the Sagittarius Dwarf Spheroidal Galaxy

Rodrigo A. Ibata

Department of Physics and Astronomy, UBC; [ibata@astro.ubc.ca](mailto:ibata@astro.ubc.ca)

Rosemary F.G. Wyse<sup>1,2</sup>

Department of Physics and Astronomy, JHU; [wyse@pha.jhu.edu](mailto:wyse@pha.jhu.edu)

Gerard Gilmore<sup>3</sup>

Institute of Astronomy, Madingley Rd. Cambridge CB3 0HA, UK; [gil@ast.cam.ac.uk](mailto:gil@ast.cam.ac.uk)

Michael J. Irwin

Royal Greenwich Observatory, Madingley Rd, Cambridge CB3 0EZ; [mike@ast.cam.ac.uk](mailto:mike@ast.cam.ac.uk)

Nicholas B. Suntzeff

Cerro Tololo InterAmerican Observatory<sup>4</sup>, Casilla 603, La Serena, Chile; [nick@ctio.noao.edu](mailto:nick@ctio.noao.edu)

### ABSTRACT

The Sagittarius dwarf spheroidal galaxy, the closest satellite galaxy of the Milky Way, has survived for many orbits about the Galaxy. Extant numerical calculations modeled this galaxy as a system with a centrally-concentrated mass profile, following the light, and found that it should lose more than one-half of its mass every 2–4 orbits and be completely disrupted long before now. Apparently the Sagittarius dwarf spheroidal, and by implication other dSph galaxies, do not have a centrally-concentrated profile for their dark matter. We develop a model in which the stars of the Sgr dwarf are embedded in a constant-density dark matter halo, representing the core of a tidally-limited system, and show that this is consistent with its survival. We present new photometric and kinematic observations of the Sagittarius dwarf spheroidal and show these data are consistent with this explanation for the continued existence of this galaxy. The Sagittarius dwarf is being tidally distorted and is tidally

---

<sup>1</sup>Institute of Astronomy, Madingley Rd. Cambridge CB3 0HA, UK

<sup>2</sup>Center for Particle Astrophysics, University of California, Berkeley, CA 95124

<sup>3</sup>Institut d'Astrophysique, 98bis Boulevard Arago, 75014 Paris, France

<sup>4</sup>Cerro Tololo Inter-American Observatory is operated by AURA, Inc. under contract to the National Science Foundation.

limited, but is not disrupted as yet. The corresponding minimum total mass is  $10^9 M_{\odot}$ , while the central mass to visual light ratio  $\sim 50$  in Solar units.

Our new photographic photometry allows the detection of main-sequence stars of the Sagittarius dwarf over an area of  $22^{\circ} \times 8^{\circ}$ . The Sagittarius dwarf is prolate, with axis ratios  $\sim 3:1:1$ . For an adopted distance of  $16 \pm 2$  kpc from the Galactic center on the opposite side of the Galaxy to the Sun, the major axis is  $\gtrsim 9$  kpc long and is aligned approximately normal to the plane of the Milky Way Galaxy, roughly following the coordinate line  $\ell = 5^{\circ}$ .

The central velocity dispersion of giant stars which are members of the Sagittarius dwarf is  $11.4 \pm 0.7 \text{ km s}^{-1}$  and is consistent with being constant over the face of the galaxy. The gradient in mean line-of-sight velocity with position along the major axis,  $dv/db$ , is  $\sim 0 \text{ km s}^{-1}/\text{degree}$  in the central regions and increases in amplitude to  $dv/db = -3 \text{ km s}^{-1}/\text{degree}$  over the outermost three degrees for which we have data. A first measurement of the proper motion of Sgr determines the component of its space velocity parallel to its major axis to be  $250 \pm 90 \text{ km s}^{-1}$ , directed towards the Galactic Plane. We model these kinematic data to determine the orbit of the Sagittarius dwarf. Our best fit model has an orbital period of  $\lesssim 1$  Gyr and has the Sagittarius dwarf spheroidal close to perigalacticon. This period is shorter, by about a factor of  $\gtrsim 10$ , than the age of the bulk of its stellar population.

*Subject headings:* dwarf spheroidal galaxies, dark matter

## 1. Introduction

The serendipitous discovery of the Sagittarius dwarf spheroidal (Ibata, Gilmore & Irwin 1994, 1995; hereafter IGI-I and IGI-II respectively) during the course of a spectroscopic study of the bulge of the Milky Way (Ibata & Gilmore 1995a, 1995b) provides an unprecedented opportunity for detailed study of the interaction between a normal large disk galaxy and one of its satellite galaxies, and of the internal structure of a dwarf spheroidal galaxy.

At least some of the dwarf spheroidal companions of the Milky Way have long been suspected to contain large quantities of dense dark matter (*e.g.*, Faber & Lin 1983; Irwin & Hatzidimitriou 1995), which has important implications for the nature of the constituents of dark halos. Most of the dwarf spheroidals contain stars with a broad range of ages and metallicities, which is unexpected in the simplest explanation for their low mean metallicities — that chemical evolution was truncated by supernovae-driven winds (*e.g.*, Sandage 1965; Dekel & Silk 1986). Further, in the currently-popular hierarchical clustering picture of structure formation, such as Cold-Dark-Matter dominated cosmologies, very significant accretion and merging of smaller systems occurs during the evolution of a normal galaxy like the Milky Way; is this on-going?

This paper presents new photometric and kinematic data that are used to constrain models of the orbit of the Sagittarius dwarf spheroidal. We propose a new model for the internal structure of the Sagittarius dwarf spheroidal, consistent with these data and with the previously apparently-surprising ability of the Sgr dwarf to have survived many perigalactic passages. This model also has significant implications for the nature of dark matter and the evolution of dwarf galaxies.

## 2. Physical Properties of the Sagittarius Dwarf Spheroidal Galaxy

### 2.1. Photometric Determination of the Spatial Extent

The first survey to map the Sagittarius dwarf (IGI-I) utilized the red horizontal branch (RHB) and clump giant stars which are members. The ‘background noise’ in this case is a combination of small number statistics and foreground Galactic stars with similar apparent magnitudes and colors. The isopleth map derived by IGI-I and IGI-II (superimposed on Figure 1 below) revealed that the Sagittarius dwarf is visible over an approximately  $10^\circ \times 4^\circ$  region centered near  $\ell = 5.6^\circ, b = -14.0^\circ$ , at the position of the globular cluster M54 (NGC 6715). However, the intrinsic rarity of RHB stars limited this detection to relatively high density regions and, as IGI-II emphasized, their outermost isopleth had detected only  $\lesssim 50\%$  of the stellar population of the Sagittarius dwarf. IGI-I additionally noted that four globular clusters were probable members of this galaxy, even though three of them lay well outside the available isopleths, further supporting an expectation that those isopleths were a lower limit on the detectable size of the Sgr dwarf. This expectation has been supported in the interim by several studies which have identified members of the Sagittarius dwarf along lines-of-sight well outside the original detection limits.

Deep CCD color magnitude diagrams of the line of sight towards the globular cluster M55 (Fahlman *et al.* 1996, Mateo *et al.* 1996) show, in addition to the expected M55 and Galactic stars, a well-defined main sequence and three RR Lyrae stars, which have magnitudes and colors expected of members of the Sagittarius dwarf spheroidal. This field is located at  $(\ell = 8.8^\circ, b = -23.0^\circ)$ , approximately  $3^\circ$  away from the outermost contour reported in IGI-I. Furthermore, a study by the DUO microlensing team (Alard 1996) in a  $5^\circ \times 5^\circ$  field centered at  $(\ell = 3^\circ, b = -7^\circ)$  has detected 313 RR Lyrae stars which have distance moduli which show them to be members of the Sgr dwarf. The surface density of these RR Lyrae stars increases away from the Galactic plane and is a broad, flat distribution: compelling evidence that what is seen is not clumpy tidal debris (as was suggested by Mateo *et al.* 1996 from their M55 observations), but simply the continuation of the isodensity contours found by IGI-I. In the direction towards the Galactic plane, these RR Lyrae stars are found up to  $b = -4^\circ$ , more than  $10^\circ$  away from the center defined by IGI-I.

At low Galactic latitudes in the direction of the Galactic Bulge, the number density and strong gradient of Galactic stars preclude using photographic survey plates to probe down to the main sequence turnoff of the Sagittarius dwarf. However, further out along its major axis in the

direction away from the Galactic plane, it is possible to probe to the full depth of the survey plates. Stars near the main sequence turnoff in the Sagittarius dwarf are much more numerous than red clump stars and they also occupy a region of the HR diagram which is significantly less contaminated by foreground Galactic stars; these two effects make it possible to obtain a more sensitive detection of the extent of the Sagittarius dwarf using main sequence stars than was obtained in the original survey of red clump stars. Isoleth maps derived from the excess of main-sequence stars which are members of the Sagittarius dwarf on four UKST fields East of the center of the Sagittarius dwarf (IIIaJ sky survey plates) are shown in Figure 1, superimposed on the original isopleth map from IGI-I.

The main sequence turnoff of Sgr occurs at a  $B_J$  magnitude of  $\approx 21.5$ , roughly a magnitude above the plate limit of UKST IIIaJ sky survey plates. Although significant geometrical vignetting is present beyond a radius of 2.7 degrees, the 5 degree separation of the survey fields — giving a 1 degree overlap between plates — ensures that the majority of the region used to construct the overall isopleth map is only marginally affected by vignetting.

As for the red clump isopleth maps, suitable comparison regions of color-magnitude space had to be defined in order to remove the varying, mainly foreground, Galactic contribution. Unfortunately, the R survey plates available for the fields of interest do not go deep enough to realistically sample the Sgr main sequence turnoff region. This restricted selection of comparison regions in color-magnitude space to limits on the  $B_J$  magnitude only. Two samples were generated for each plate: a comparison region in the magnitude range 19.5 – 21.0; and a main sequence reference region from 21.5 – 22.5. Clearly, there is some contamination in the comparison sequence from Sgr members but it is a relatively small fraction,  $<5\%$ , compared to the proportion of Sgr members in the reference region,  $\approx 25\%$ . The individual Sgr isopleth maps are then constructed by subtracting a suitably scaled, and smoothed version of the comparison map from the reference map. The extra smoothing of the comparison map (only), at a scale of  $\approx 30$  arcmin, is used to suppress additional quantization noise being added in quadrature to the desired signal.

The Galactic gradient in these fields is very large. For example, counting all stellar images from  $B_J = 18$  to the plate limits, typically reveals an image density ranging from  $10 \text{ arcmin}^{-2}$  at one plate edge to  $20 \text{ arcmin}^{-2}$  at the opposite edge. Of these on average around 10% will be Sgr members, mostly belonging to the main sequence.

The effective resolution of the isopleth maps at  $\approx 10$  arcmin, is a compromise between the desire to probe the detailed structure of Sgr and the need to keep the quantization noise at a manageable level. However, the much larger numbers of Sgr main sequence members per unit area (contour intervals are  $\approx 1 \text{ arcmin}^{-2}$ ) compared to the earlier red clump isopleth maps, enable us to probe much further out along both major and minor axis directions, due to the reduction in random noise. There are various systematic effects present that preclude combining all four of the individual maps in a straightforward quantitative fashion, including lack of deep photometric calibrators and complex systematic field effects (in addition to vignetting) present on the plates

at the  $\pm 0.1$  magnitude level. This coupled with the natural variation in plate limiting magnitude, make selecting a consistent sample of Sgr main sequence stars very difficult and help to explain why the individual isopleth maps outlined in Figure 1 do not join up smoothly. In spite of these caveats the maps are accurate enough to reveal the general shape and extent of Sgr, although we caution that the full extent of Sgr has to be greater than the apparent boundaries in the combined isopleth map.

Combining all this star count information, the Sagittarius dwarf spheroidal has been detected down to  $b = -26^\circ$  along the E side of its major axis. Fields further out do not show any significant detection of stars which are likely to be main sequence members of the Sagittarius dwarf. The last detected isopleth in Figure 1 corresponds to a surface density of  $\approx 1 \text{ arcmin}^{-2}$ , which is a factor  $\sim 10$  below the peak surface density near M54. Isopleths constructed from either main-sequence or red horizontal branch stars are consistent with a system which is to first order symmetric about a line of constant latitude drawn through the location of M54 ( $\ell = 5.6^\circ, b = -14.0^\circ$ ). The detection of the DUO RR Lyrae stars in the Sagittarius dwarf within  $\sim 5^\circ$  of the Galactic plane is consistent with this symmetry, although stronger statements await better calibration of the relative surface densities of RR Lyrae and main sequence stars in the different fields studied. Along the minor axis, our isopleths derived from main sequence stars provide a detection from  $l = 3^\circ$  to  $l = 11^\circ$  degrees. Thus, the Sagittarius dwarf spheroidal has been detected over an area of  $22 \times 8$  degrees in extent, encompassing all previous measurements. This area includes the positions of the four globular cluster members. We caution however, that to obtain these measurements of the extent and shape of the Sagittarius dwarf, we have had to patch together different data sets, each obtained with different selection criteria, and most involving a difference between regions of color-magnitude space which isolates the Sagittarius dwarf only in a statistical way. The shape, extent, and particularly the normalization of the contours that we have derived are therefore necessarily uncertain. Additionally, it should be noted that the statistical significance of the high frequency structure in the isophotal contours is marginal. Real substructure is not physically plausible, given the short internal crossing times.

The apparent flattening of the Sagittarius dwarf is  $\sim 3:1$ , corresponding to an ellipticity of  $\sim 0.7$ . Thus the Sagittarius dwarf has significantly higher projected ellipticity than the other dSph companions to the Milky Way, which have projected ellipticities  $\lesssim 0.3$  (with the exception of Ursa Minor, which has ellipticity  $\sim 0.5$ , Irwin & Hatzidimitriou 1995). Indeed, the Sagittarius dwarf is as flat as the most flattened elliptical galaxies.

## 2.2. Surface Brightness Profile of the Sagittarius dwarf

The most robust, model-independent quantities that can be determined from the isophotal contours are the radius along the minor axis at which the surface brightness has fallen to half of its central value,  $R_{HB}$  and the limiting radius,  $R_{lim}$ , again along the minor axis. The contours shown here give values of  $R_{HB} \sim 1.25^\circ$ , and  $R_{lim} \sim 4^\circ$ . The half-brightness radius is a lower limit

to the characteristic radius of a King model fit,  $r_o$  (see, *e.g.*, Binney & Tremaine 1987) and the limiting radius will approximate the tidal radius,  $r_t$ . Using the ratio  $R_{HB}/R_{lim}$  to estimate the corresponding King model concentration parameter gives  $c \sim 0.5$ . This is a typical value derived for the dSph companions to the Milky Way (Irwin & Hatzidimitriou 1995, their Table 4 — Carina, Draco, Leo II and Ursa Minor all have  $c \sim 0.5$ ).

The total luminosity of the Sagittarius dwarf spheroidal has been estimated by IGI-II from the relative frequency of the RHB, giving  $L_V \sim 10^7 L_\odot$ , and by Mateo *et al.* (1996), who derive  $L_V \sim 2 \times 10^7 L_\odot$ .

## 2.3. Distance and 3-dimensional Shape

### 2.3.1. Line-of-Sight Depth

**Field Stars** The dispersion among the apparent magnitudes of the RR Lyrae stars detected in the Sagittarius dwarf may be used to give an upper limit to the line-of-sight depth. Alard (1996) finds that the extinction-corrected magnitude distribution of RR Lyrae variables may be fit by a Gaussian with  $\sigma = 0.3$  mag. This dispersion contains contributions from photometric errors, uncorrected local variations in extinction and a possible range in RR Lyrae metallicities in the sample. Formally, these effects explain the whole observed dispersion. However, interpreting the FWHM ( $2.34\sigma$ ) of this distribution as an absolute upper limit to the differential distance modulus of the Sagittarius dwarf yields an upper limit to the line of sight extent of  $\lesssim 8$  kpc (for an assumed mean distance of 25 kpc).

Another estimate of the line-of-sight depth at a point can be obtained from the magnitude spread of the more numerous red clump stars over a small field. Stars belonging to the red clump in the CMD represent the core-He-burning phase of intermediate-mass and/or intermediate-metallicity stars (*e.g.*, Chiosi, Bertelli & Bressan 1992). Some intrinsic spread in the red clump is expected, even in a uniform age, uniform abundance stellar population (see Lee, Demarque & Zinn 1994, their Figure 1). Nevertheless, even in a mixed age, mixed abundance population the magnitude spread across the red clump provides an upper limit to the distance spread along the line of sight. We have extracted stars of the appropriate color and magnitude to be red clump giants in the Sagittarius dwarf spheroidal from the CCD data of Sarajedini & Layden (1995); these data are from a  $7' \times 7'$  field, so problems due to patchy extinction and variations in mean distance of these stars should be minimized.

Figure 2 shows the distribution in magnitude of field stars well away from the line-of-sight to the globular cluster M54 (projected distance of  $12'$ ), and selected to lie in the narrow color strip  $1.05 < V - I < 1.17$ . There is a narrow, local maximum in the bin centered on  $V = 18.25$ . This distribution is modeled in the range  $18.0 < V < 18.5$  as follows: the smooth and rising distribution of ‘non-red-clump’ stars (foreground Galactic stars and Sgr giants and subgiants) is fit by a straight

line segment to a 0.2 mag wide bin near  $V = 18.0$  and  $V = 18.5$ , while the red clump ‘hump’ is modeled with a Gaussian superimposed on this sloping background. The maximum-likelihood fit of the (unbinned) data to this combined model is superimposed on Figure 2; the Gaussian has a dispersion of 0.04 magnitudes.

The width of the apparent magnitude distribution of these stars results from a convolution of intrinsic spread due to distance, age and metallicity differences, together with the photometric error ( $\sigma_V = 0.01$  near  $V = 18$ ), so it is an upper limit to the intrinsic dispersion in distance modulus. Adopting a conservative dispersion of 0.04 mag, giving a FWHM of 0.1mag, the corresponding dispersion in line of sight distance, again for an assumed mean distance of 25 kpc, is  $\Delta D = 1.2$  kpc.

**The globular clusters** There are 4 globular clusters unambiguously belonging to the Sagittarius dwarf, based on commonality of distance, radial velocity and celestial coordinates (see Table 1; references are given in the text where appropriate). The variation in the cluster distance moduli can be used to derive an upper limit to the line-of-sight depth of the Sagittarius dwarf. Da Costa & Armandroff (1995) derive the following reddening-corrected distance moduli: M 54 – 17.14; Ter 8 – 16.69; Ter 7 – 16.72 and Arp 2 – 17.34.<sup>5</sup> These values provide a mean cluster distance modulus of 17.00, with a dispersion of 0.32 mag, corresponding to  $25 \pm 4$  kpc. The same range of distance moduli (with a small zero-point offset) is derived by Chaboyer, Demarque & Sarajedini (1996) for Ter 7, Ter 8 and Arp 2 (they do not have M 54 in their sample). This dispersion is remarkably similar to the spread in RR Lyrae apparent distance moduli (Alard 1996), albeit that the globular clusters are spread over  $\sim 8$  degrees on the sky.

Thus, the globular cluster distance data are consistent with those of the field stars, but do not provide more precise constraints with extant data.

**Three-Dimensional Shape** The red clump stars provide the most robust estimate of the line-of-sight depth, and from above the half-brightness depth is 1.2 kpc. This is remarkably similar to the minor axis parameters derived from the isopleth maps of §2.1, where the half-brightness minor axis diameter, for a distance of 25 kpc, is  $2 \times 550$  pc. The 3-dimensional shape of the Sgr dwarf is thus a prolate spheroid with axis ratios 3:1:1 and a long axis approximately in the plane of the sky and at constant longitude.

---

<sup>5</sup>We have corrected the distance modulus for Arp 2 to take account of the fact that the apparent magnitude of the Horizontal Branch that da Costa and Armandroff used was the ZAHB value,  $V_{HB} = 18.30$ , as given by Buonomano *et al.* (1995a), whereas, as pointed out by Chaboyer, Demarque & Sarajedini (1996), the mean value of the apparent magnitude of the horizontal branch is the quantity that should be compared with the theoretical absolute magnitude of the HB quoted (which is not the ZAHB). This mean value is given by the last authors as 18.18.

### 2.3.2. Mean Distance Across the Face of the Sagittarius Dwarf Spheroidal

IGI-I and IGI-II derived the distance to the Sagittarius dwarf by assuming that the red clump stars have the same intrinsic luminosity and color as those in the Small Magellanic Cloud (SMC) and matching SMC and Sgr color-magnitude data to derive the relative distance and reddening. Adopting 57 kpc as the (standard) distance for the SMC provides a distance to the Sagittarius dwarf of  $24 \pm 2$  kpc, corresponding to a distance of the center of the Sagittarius dwarf from the Galactic center of  $16 \pm 3$  kpc for an adopted Solar Galactocentric distance of 8 kpc.

A similar estimate results from analysis of the apparent magnitude of the  $\sim 10$  RR Lyrae member stars identified by the OGLE microlensing experiment group (Mateo *et al.* 1995a; Mateo *et al.* 1995b). The significant improvement in statistics provided by the DUO microlensing experiment, which has identified 313 RR Lyrae candidates in the Sagittarius dwarf (Alard 1996), again yields a mean distance of  $24 \pm 2$  kpc, for the field centered at  $\ell = 3^\circ$ ,  $b = -7^\circ$ , for an adopted RR Lyrae (*ab* type) absolute magnitude  $M_{B_J} = 0.79$ .

In principle the most precise distance at present can be derived from the combination of the DUO RR Lyrae data and the distances to the four globular cluster members (modulo the line-of-sight depth for the cluster system, as discussed below). In the case of the RR Lyraes, however, one is limited by their unknown chemical abundances and, in both cases, one is further limited by lack of knowledge of the appropriate chemical abundance-luminosity calibration for horizontal branch stars, since the internal chemical abundance range in the Sagittarius dwarf apparently spans at least 1.5dex. The most detailed discussion is in Sarajedini & Layden (1995, their Table 3), where they derive distances for M54 and for the field stars of the Sagittarius dwarf spheroidal under a range of adopted relationships for the absolute magnitude of the horizontal branch. They obtain distances covering the range from 25 kpc to 29 kpc, with the closer distance preferred by the most recent HB calibrations. The same range of distances is derived from main sequence turn-off fits for Sgr stars by Fahlman *et al.* (1996).

Presently, there are too few confirmed RR Lyrae members to provide useful information on differential distances over the dwarf. However, red clump stars are numerous in the Sagittarius dwarf, and can be used as standard candles, assuming that there are no systematic variations in stellar population with position over that galaxy. Twenty-six fields along the major axis of the Sagittarius dwarf were observed in V and I on the 1.5m telescope at CTIO (27 March 1996) with the Tek1024 CCD. A thorough description of the reductions and analysis of these data will be presented in a subsequent contribution. However, it is useful for the present discussion to mention the resulting distance constraints. Figure 3 shows the color-magnitude diagram of one of the major axis fields at ( $\ell = 15.48^\circ$ ,  $b = -15.09^\circ$ ). Assuming that most of the reddening is due to foreground dust, the difference in reddening between a given field and the template field (chosen to be the off-cluster field of Sarajedini & Layden 1995) can be estimated by finding the difference in  $V - I$  color of the blue edge of the disk sequence (seen clearly in Figure 3 at  $V - I \sim 0.8$ ,  $V < 17.5$ ). All of the photometry was extinction-corrected in this way to the extinction of the template field.



The V magnitude of the peak of the red clump was fit using the technique described for Figure 2. The uncertainties of these magnitudes were derived from bootstrap resampling and include the statistical uncertainties in the extinction correction. Assuming  $M_V(\text{RR}) = 0.15[\text{Fe}/\text{H}] + 1.01$  (Carney, Storm & Jones 1992), and the following parameters from Sarajedini & Layden (1995):  $[\text{Fe}/\text{H}]_{\text{Sgr}} = -0.5$ ,  $M_V(\text{red clump}) = M_V(\text{RR}) + 0.11$  and  $A_V = 0.403$  (for the template field) gives the heliocentric distances displayed in Figure 4.

A least squares fit of a straight line to the data presented in Figure 4 has a slope of  $0.03 \pm 0.05 \text{ kpc/degree}$ , so an adequate working statement for present use is that the extant data are consistent with a distance to the Sagittarius dwarf of  $\sim 25 \pm 2 \text{ kpc}$ , with no significant evidence for any variation in distance along the major axis.

This value of the distance translates the angular half-brightness radius estimated above into a linear half-brightness radius on the minor axis of  $R_{HB} \sim 550 \text{ pc}$ . Similarly, the limiting minor axis radius is  $R_{lim} \sim 1.7 \text{ kpc}$ . The Sagittarius dwarf spheroidal is visible over a region with diameter  $22^\circ$  along the major axis and  $8^\circ$  diameter along the minor axis. At a heliocentric distance of  $25 \text{ kpc}$  this corresponds to a major axis diameter of  $9.6 \text{ kpc}$  and a minor axis diameter of  $3.5 \text{ kpc}$ .

## 2.4. Metallicity and Age

The discovery observations of IGI-I allowed them to derive (low-precision) metallicities for Sgr K and M giants from the equivalent widths of the Mgb feature. They determined the mean  $[\text{m}/\text{H}]$  to be  $\approx -1.1$ . The existence of an intrinsic metallicity spread was deduced from the color-magnitude diagram by IGI-II, who also deduced that the Sagittarius dwarf has a significant intermediate-age stellar population based on the strong red clump and on the existence of carbon stars.

Mateo *et al.* (1995a) confirmed, from the distribution of the turn-off stars in their deep (V – I,V) data, that the dominant stellar population of Sgr has an age of 10 Gyr. They deduced from the color of the giant branch that the mean metallicity is  $[\text{Fe}/\text{H}] \sim -1.2$ . Fahlman *et al.* (1996) were able to fit their more precise photometry of main-sequence stars in the Sagittarius dwarf with isochrones which range, in a coupled determination of abundance and age ( $[\text{Fe}/\text{H}]; T$ ), between ( $[\text{Fe}/\text{H}] = -0.8; T = 10 \text{ Gyr}$ ) and ( $[\text{Fe}/\text{H}] = -1.2; T = 14 \text{ Gyr}$ ).

Sarajedini & Layden (1995) identified, in their photometric study, three different stellar populations in the Sgr dwarf. These are a metal-poor component, typified by M54, with  $[\text{Fe}/\text{H}] = -1.8$ ; an intermediate-metallicity component with  $[\text{Fe}/\text{H}] = -1.3$ , and a dominant, relatively metal-rich component with  $[\text{Fe}/\text{H}] \sim -0.5$ .

The Sgr globular clusters all have spectroscopic metallicity determinations, (see Table 1) in each case based on the infrared calcium triplet strengths for  $\sim 5$  evolved stars. These metallicities are: M54,  $[\text{Fe}/\text{H}] = -1.55$ ; Ter 8,  $[\text{Fe}/\text{H}] = -1.99$ ; Ter 7,  $[\text{Fe}/\text{H}] = -0.36$  and Arp 2,

$[\text{Fe}/\text{H}] = -1.70$  (eg. da Costa & Armandroff 1995). An alternative (photometric) metallicity determination for Ter 7 is  $[\text{Fe}/\text{H}] \sim -1$  (Buonanno *et al.* 1995b; Sarajedini & Layden 1996). [This is an example of the fact that empirically, spectroscopic metallicity determinations using the Ca triplet have been found to agree with those based on the giant branch color only for metallicities below one-tenth of the solar value; see Buonanno *et al.* .] Adopting the photometric metallicity for Ter 7 results in a mean (unweighted) globular cluster metallicity of  $\sim -1.6$  dex, some  $\gtrsim 0.5$  dex more metal-poor than the field star population, and a spread of  $\sim 1$  dex, similar to that of the field stars. (M 54 dominates a luminosity-weighted metallicity distribution for the globular clusters, giving a mean that is only slightly more metal-rich than the unweighted mean.)

For comparison, the Fornax dwarf spheroidal galaxy has a mean field-star metallicity of  $[\text{Fe}/\text{H}] = -1.4$  (Buonanno *et al.* 1985; Beauchamp *et al.* 1995),  $\sim 0.4$  dex more metal-rich than the average of its cluster population,  $[\text{Fe}/\text{H}] = -1.8$ . This difference is approximately the same as that discussed above for the Sagittarius dwarf. The full range of the field star metallicities in Fornax is  $\sim 0.8$  dex (Beauchamp *et al.* 1995), approximately the same as that of the five globular clusters of Fornax (see also da Costa & Armandroff 1995), and again similar to the metallicity spreads in the field and globulars of Sgr. The mean age and age range of the field stars and globulars of Fornax are considerably different from those of the Sagittarius dwarf spheroidal, however. All studied globulars of Fornax are consistent with an old age, while the Fornax field stars show a dominant population that is less than  $\sim 5$  Gyr old, with a range extending down to  $\sim 1$  Gyr (Beauchamp *et al.* 1995).

The presence of RR Lyrae stars in a stellar system is an indicator of an old population. Theoretical quantification of ‘old’, by application of stellar evolution models to horizontal branch morphology, remains uncertain. Observational calibration, by the detection of RR Lyrae stars in a range of globular clusters for which relative age estimates are available, is feasible (*cf.* Olszewski, Schommer & Aaronson (1987) for an earlier discussion of this approach). IC 4499 is the youngest metal-poor globular cluster ( $[\text{Fe}/\text{H}] \sim -1.5$ ) with a very substantial population of RR Lyrae variables; indeed IC 4499 has one of the highest specific frequencies of RR Lyrae stars (Suntzeff, Kinman & Kraft 1991; Sarajedini 1993). On the age scale which has the canonical ‘old’ halo being in the mean 17 Gyr old (Chaboyer, Demarque & Sarajedini 1996, their favored calibration of the RR Lyrae luminosity being  $M_{V,RR} = 0.20[\text{Fe}/\text{H}] + 0.98$ ), IC 4499 has an age of  $\sim 12$  Gyr, in agreement with the conclusions of Ferraro *et al.* (1995). The Sgr clusters with ages estimated by Chaboyer *et al.* are Ter 7,  $\sim 9$  Gyr on their scale; Arp 2,  $\sim 14$  Gyr; and Ter 8,  $\sim 19$  Gyr. Arp 2 has 2 RR Lyrae stars detected, plus 12 HB stars blueward of the instability strip and none redward (Buonanno *et al.* 1995a). Richer *et al.* (1996) find that Arp 2 is  $\sim 5$  Gyr younger than their fiducial globular cluster at that metallicity (NGC 7492 with  $[\text{Fe}/\text{H}] = -1.5$  and an estimated absolute age of 15 Gyr), while Ter 7 is  $\sim 4$  Gyr younger than its fiducial at that metallicity (NGC 104 with  $[\text{Fe}/\text{H}] = -0.7$  and an estimated absolute age of 14 Gyr).

A robust conclusion, consistent with both analyses of globular cluster ages, is that an RR Lyrae population can occur in stellar systems with metallicities  $\sim -1.5$  dex that are as much

as  $\sim 5$  Gyr younger than the classical old halo. Thus the detection of RR Lyrae stars in the Sagittarius dwarf spheroidal is indicative of a population of age greater than  $\sim 10 - 12$  Gyr.

In summary, the extant data show that globular clusters of the Sagittarius dwarf are more metal poor than its field stars, but cover a very wide age range. The Sgr field stars are predominately of comparable age to the younger globular clusters,  $\sim 12$ Gyr, but extend to sufficiently young ages to allow carbon stars to exist and to sufficiently old ages to allow a substantial RR Lyrae population. The field stars also cover a very wide range of metallicity. The distribution function of metallicities in Sgr remains poorly determined. Most observations, however, determine a mean abundance more metal rich than  $-1$  dex, with a range of  $\sim 1$  dex. The Sagittarius dwarf spheroidal contains the most metal-rich stars of any of the dSph companions of the Milky Way.

In §5 we use these limits on the age of the stellar populations in Sgr to constrain its survival against destruction by Galactic tides.

## 2.5. Radial Velocities

Two complementary sets of kinematic data for member stars in the Sagittarius dwarf have been obtained.

Spectroscopic data from three observing runs on the 3.9m Anglo-Australian Telescope (AAT) determine the mean kinematics of the Sagittarius dwarf. The first two of these runs (9–13 July 1990, 3–8 August 1993) were part of a survey which aimed to determine the kinematic and abundance distributions of the Galactic Bulge. The goal of the third AAT run (1–4 August 1994) was specifically to measure the gradient in the mean line-of-sight velocity over the face of the Sagittarius dwarf spheroidal and to provide confirmed member stars for higher-resolution spectroscopic study at CTIO. The candidate Sgr giant and asymptotic giant branch members were selected from CMDs constructed from scans of United Kingdom Schmidt Telescope IIIaJ and IIIaF survey plates using the Automatic Plate Measuring (APM) machine (Kibblewhite *et al.* 1984). In sparsely populated regions, such as around Ter 8, all stars whose location in the CMD was consistent with that of the Sgr giant branch were observed. The AAT observations used the AUTOFIB multi-object fiber spectrograph system. A detailed description of the observational details, the data reduction and resulting velocity and abundance precision, together with a detailed description of the APM photometry, is presented by Ibata & Gilmore (1995a). The velocity data resulting from the July 1990 and August 1993 runs are listed in Ibata & Gilmore (1995a), their Table B1. The data from the August 1994 run are presented in Table 2.A, which contain accurate coordinates, APM photometry and AAT heliocentric radial velocities for 229 stars. Repeat observations of the same star are indicated by a “ditto” in the coordinate and photometry columns.

Since the internal velocity dispersion of dSph galaxies is comparable to the accuracy provided

by AUTOFIB (the velocity accuracy of the sample from Ibata & Gilmore 1995a is  $\sim 12 \text{ km s}^{-1}$ ), complementary observations were obtained with the ARGUS multi-fiber setup at the 4m Cerro Tololo Interamerican Observatory (CTIO) (2-6 August 1994) feeding the bench-mounted echelle spectrograph. The advantage of this instrument over AUTOFIB is a significant increase in the precision of individual velocity measurements, which however comes at the cost of lower throughput and reduced multiplexing (24 fibres instead of 64). See Suntzeff *et al.* (1993) for a comprehensive description of ARGUS and ARGUS data reduction procedures. The Blue Air Schmidt camera, 5186r<sup>1/4</sup>A filter and  $1200 \times 200$  CCD were used for the echelle observations. Due to a malfunction in the CCD controller, the read noise was exceptionally high,  $6.8 \pm 0.6e^-$ , resulting in an average S/N  $\sim 10$  in the  $\sim 1$  hour exposures. Stars from M4, M11, 47 Tuc and NGC 288, in addition to the IAU velocity standard star BS 9014, were observed for use as velocity templates.

The resulting velocity data are presented in Table 2.B, which contains accurate coordinates, APM photometry, CTIO heliocentric radial velocities and Tonry-Davis crosscorrelation R values (Tonry & Davis 1979) for 270 stars. Repeat observations of the same star using different fiber setups are indicated by a “ditto” in the coordinate and photometry columns. Some spectroscopic integrations were divided into two exposures; where applicable, an extra entry in the table lists the absolute value of the velocity difference between measurements on the two exposures. Entries marked with ellipses denote unavailable data.

The fields observed extend  $\sim 10$  degrees along the major axis of the Sagittarius dwarf and are identified in Figure 5. Identification of members of Sgr is straightforward from the kinematic data, as the Sagittarius dwarf is offset in mean velocity from Galactic bulge stars — the primary contaminant — by  $\sim 150 \text{ km s}^{-1}$  (*cf.* Fig 4 of IGI-II). Thus, we select as members of the Sgr dwarf all giant stars with heliocentric radial velocities satisfying  $100 \text{ km s}^{-1} \leq v \leq 180 \text{ km s}^{-1}$ .

Eighty-seven stars were observed at both CTIO and the AAT and provide a check on both the velocity zero points and the internal precision of the AAT data. The distribution of differences between the repeat measurements was found to be Gaussian. The mean difference in the sense (AAT-CTIO) is  $+1.4 \text{ km s}^{-1}$ , while the dispersion is  $6.3 \text{ km s}^{-1}$ , which is dominated by the AAT measuring error.

### 2.5.1. Kinematic Results

The Sagittarius dwarf spheroidal covers such a large angular extent that there is a small but systematic variation across its surface in the projected component of the space velocity of the Sun. We thus convert the heliocentric velocities of Table 2 to values which would be seen by an observer at the position of the Sun, but in the reference frame in which the Local Standard of Rest at the Sun is orbiting the Galactic center with a velocity of  $220 \text{ km s}^{-1}$ . We define this to be ‘Galactocentric’ radial velocity,  $v_{\text{GAL}}$ .

The peculiar velocity of the Sun relative to the Local Standard of Rest is assumed to be  $v_{\text{pec},\odot} = 16.5 \text{ km s}^{-1}$  in the direction  $\alpha_{1900} = 18.0^\circ$ ,  $\delta_{1900} = 30^\circ$ . Defining  $v_{\text{HEL}}$  to be the observed heliocentric radial velocity of a star at Galactic coordinates  $(\ell, b)$ ,  $v_{\text{pec},\odot,(\ell,b)}$  to be the component along the line of sight to the star of the peculiar velocity of the Sun and  $v_{\text{rot,LSR}} = 220 \text{ km s}^{-1}$  to be the circular velocity of the LSR at the Sun’s location, then the ‘Galactocentric’ radial velocity of that star is

$$v_{\text{GAL}} = v_{\text{HEL}} + v_{\text{pec},\odot,(\ell,b)} + 220 \text{ km s}^{-1} \sin \ell \cos b. \quad (1)$$

The Galactocentric radial velocity data, plotted against Galactic latitude, are shown in Figure 6. The radial velocities of the 4 globular clusters which are members of Sgr are also indicated in Figure 6 and lie well within the intrinsic dispersion of the kinematic data for Sgr field stars.

To quantify the variations in mean velocity and velocity dispersion in these data, each of the eight fields observed at the AAT, four of which were also observed at CTIO, was considered separately. A maximum-likelihood routine was used to fit Gaussian functions to the data in each of these fields; the uncertainties on the mean and dispersion were calculated by bootstrap resampling of the data. The fitted parameters for each field are given in Table 3. The histograms of the CTIO velocity data in fields f1, f5, f6 and f7 are shown in the upper row of panels in Figure 7 with the fitted functions superimposed. The lower two rows of panels in Figure 7 show histograms of the AAT velocity measurements. The data show, along the major axis, an increase in the mean velocity of  $\sim 10 \text{ km s}^{-1}$  over the  $5^\circ$  from field f1 to f4 and then an approximately constant mean velocity until the end of the data in field f8. Though the data do not span a wide range in distance along the minor axis, there is no evidence for significant variations in mean velocity in that direction (see below).

The Gaussian parameters fit to these data with their corresponding uncertainties are displayed in Figure 8 as a function of position along the major axis of the Sagittarius dwarf spheroidal and are listed in Table 3. The mean velocities are shown in the left hand panel of Figure 8. In each subfield, the mean and its uncertainty for the AAT and CTIO data are shown separately. The velocity dispersions derived from the CTIO echelle data are given in the right hand panel. The mean velocity shows a smooth rise of  $17 \pm 5 \text{ km s}^{-1}$  from  $b = -26^\circ$  to  $b = -20^\circ$  ( $\sim 3 \text{ km s}^{-1}/\text{degree}$ ) and then remains constant, within the uncertainties, to  $b = -12^\circ$  (see also Table 3).

The central velocity distribution (f7) is fit by a Gaussian with a dispersion of  $11.4 \pm 0.7 \text{ km s}^{-1}$ . This value is consistent with the  $12 \text{ km s}^{-1}$  dispersion obtained using just the 4 globular clusters (da Costa & Armandroff, 1995).

The velocity dispersion of members of the Sagittarius dwarf spheroidal at  $b = -25^\circ$  is equal to the central velocity dispersion  $\sigma = 11 \text{ km s}^{-1}$ . Indeed, the velocity dispersion is invariant over the face of the Sagittarius dwarf spheroidal to within the uncertainties, as quantified in Table 3. Further, within the precision allowed by the small sample, the distribution of velocities is Gaussian

in each of our fields.

## 2.6. Minor Axis Rotation

Assuming that the line  $\ell = 5^\circ$  corresponds to the major axis of the Sagittarius dwarf spheroidal, we investigate the evidence for rotation around this axis (*i.e.*, minor axis rotation). Such streaming has been observed in Ursa Minor (Hargreaves, Gilmore, Irwin & Carter 1994b), probably an effect of preferential tidal stripping. The kinematic data of Tables 2.A, 2.B, and Table B1 of Ibata & Gilmore (1995a), were divided up into three groups spanning the ranges of Galactic latitude  $b > -17.5^\circ$ ,  $-22.5^\circ < b < -17.5^\circ$  and  $b < -22.5^\circ$ . These velocity data are displayed as a function of Galactic longitude in Figure 9. The best fitting straight lines to these  $\ell - v$  data are superimposed on the diagrams. The slopes of these lines are  $-0.6 \pm 1.0$  km/s/degree,  $0.9 \pm 2.3$  km/s/degree and  $-3.5 \pm 2.9$  km/s/degree. Thus, to within the uncertainties, the fits are all consistent with no minor axis rotation. This result is insensitive to the choice of center of the Sagittarius dwarf spheroidal.

## 2.7. Proper Motion

First epoch plates were taken in the early 1950’s as part of the Palomar Sky Survey. The E (red) survey plates are well matched to recent UKST R plates and provide the proper-motion information covering a 30+ year baseline. The UKST IIIaJ sky survey plates were used to provide information on colors, to help discriminate between foreground stars and stars likely to be members of the Sagittarius dwarf spheroidal.

The preliminary proper motion of the Sagittarius dwarf spheroidal has been estimated with respect to Galactic foreground stars (a full account of this work will be published elsewhere). At  $l = 5^\circ$ ,  $b = -15^\circ$ , three Galactic populations need to be considered: the Galactic bulge, at an effective distance of  $\sim 10$  kpc, and thin and thick disk stars with maximum volume contributions at distances of  $\sim 2$  kpc and  $\sim 6$  kpc, respectively.

On these photographic CMDs, the red clump/RHB is the best-defined and populated part of the Sagittarius dwarf spheroidal and was used to pick out the members. The RHB has a color equivalent to K stars ( $B - V = 1.0$ ) and, in order to minimize the need for complex color- and magnitude-dependent astrometric corrections, the reference objects were selected over a narrow grid of colors and magnitudes centered around those of the Sgr RHB. K dwarfs in the Galactic bulge have R magnitudes  $> 20$  and Bulge K giants have R magnitudes  $< 15$ , implying that neither population is a significant contributor. Likewise, the thick disk K stars do not make a significant contribution to the numbers. The dominant Galactic component in and around the RHB stars are thin disk K dwarfs with expected R magnitudes of 17–18.

The expected reflex solar motion for both disk K stars and members of Sgr in this direction is parallel to the plane of the Galactic disk and, thus, is perpendicular to the direction of elongation of Sgr. This means that any apparent motion of member stars parallel to the direction of the major axis of the Sagittarius dwarf spheroidal is dominated by the orbital motion of Sgr.

The Galactocentric transverse orbital motion of the Sagittarius dwarf spheroidal is  $2.1 \pm 0.7$  mas/yr, *i.e.*,  $250 \pm 90$  km/s, towards the Galactic Plane. In terms of Galactic [U,V,W] velocities (with a convention of U positive in the radial direction towards the Galactic Center, V in the direction of Galactic rotation and W northwards) and assuming that the unknown proper motion of the Sagittarius dwarf parallel to the Galactic Plane is zero, the total space motion of the Sagittarius dwarf is then [232, 0:, 194]. The U and W components are well-constrained, with errors  $\pm 60$  km/s, while a secure value for the V component awaits the use of an extragalactic reference frame. This is a total velocity amplitude of  $\sim 300$  km/s.

### 3. The Orbit of Sgr

The kinematic data presented above allow a new determination of the possible orbits of the Sagittarius dwarf. The important physical parameters of the Sagittarius dwarf which constrain its orbit are:

- (i) the distance, which is well-determined in the central field near M54 and reasonably constrained across its face;
- (ii) the spatial variation of the mean radial velocity, which is extremely important and now moderately well determined;
- (iii) the internal dispersion profile, now moderately well determined;
- (iv) the proper motion, which now has a preliminary measurement.

The mass of the Sagittarius dwarf is not important for constraining the orbit, provided it is low enough that dynamical friction has not substantially modified the orbit over an orbital period. This limit is  $4 \times 10^9 M_{\odot}$  at the current Galactocentric distance; we argue below that this is satisfied.

In principle, the best way to calculate the orbit of the Sagittarius dwarf spheroidal is to construct a self-gravitating N-body model and to follow its evolution in the Galactic potential. The model would be evolved until the present time, at which point the projected velocities of the particles and projected density of the model would be compared to observations. Successive refinements to the assumed initial position, initial velocity and initial mass distribution of the model would allow iteration towards a best-fitting solution. However, this approach is beyond the scope of the present paper.

The present velocity and distance profiles across the major axis of the Sagittarius dwarf probe the projected velocity and distance to the center of mass of the dwarf as it proceeds along its orbit. We explore an assumption which greatly simplifies the orbit determination: that stars in the

Sagittarius dwarf can be regarded as test particles which all move on the same orbit. Numerical simulations (see §4 below) show that Galactic tides force a satellite galaxy into a prolate shape, and at pericenter the satellite’s longest axis is aligned along its orbit. However, this alignment with the orbit is only approximate, since the internal self-gravity in the dwarf will act to decelerate stars that lead the center of mass to lower energy orbits, and to accelerate stars that trail the center of mass to higher energy orbits. The prolate dwarf is thereby rotated about its center of mass such that the leading edge drops towards the Galactic center (see e.g., Oh *et al.* 1995). However, this is a small effect. The self-gravity also affects the major axis velocity profile. In the limiting case, the Sagittarius dwarf could be considered as a rigid, tumbling bar, in which the apparent velocity at each point along the major axis is the sum the projected velocity of the center of mass and the local streaming velocity. We consider the validity of our approach in §5.3 below, where we show the likely amplitude of the failures of our simplifying assumption is small. The mean velocity profiles of our two extreme models turn out to be similar, which suggests that the velocity gradient across the dwarf is primarily determined by the potential of the Milky Way rather than by the rigidity of the dwarf.

Following Johnston *et al.* (1995), we model the Milky Way galaxy by the sum of three rigid potentials, with the disk component described by a Miyamoto-Nagai model (Miyamoto & Nagai 1975)

$$\Psi_{disk} = -\frac{GM_{disk}}{(R^2 + (a + \sqrt{z^2 + b^2})^2)^{1/2}}, \quad (2)$$

the combined halo and bulge by a spherical Hernquist potential (Hernquist 1990),

$$\Psi_{sphere} = -\frac{GM_{sphere}}{(r + c)}, \quad (3)$$

and the dark halo by a logarithmic potential

$$\Psi_{halo} = v_{halo}^2 \log(r^2 + d^2). \quad (4)$$

In these expressions,  $R$  and  $z$  are in cylindrical coordinates, while  $r$  is the radial distance in spherical coordinates;  $M_{disk} = 1.0 \times 10^{11} M_{\odot}$ ,  $M_{sphere} = 3.4 \times 10^{10} M_{\odot}$ ,  $v_{halo} = 128$  km/s,  $a = 6.5$ ,  $b = 0.26$ ,  $c = 0.7$  and  $d = 12.0$ , all in kpc.

We will first obtain constraints on the orbit of the Sagittarius dwarf assuming that there are no systematic internal streaming motions (essentially neglecting rotation and expansion) or figure rotation (tumbling). With this, the apparent mean velocity at each point along the major axis of Sgr may be modeled by the true space velocity of a test particle at the corresponding point on the orbit.

The test particle is started off at the present position of M54, using 25 kpc as the value for the distance of the Sagittarius dwarf at this point. We explicitly assume zero transverse velocity perpendicular to the direction of elongation of Sgr, as in §2.7 above. The other two components of space motion are specified, by initial guesses. The equations of motion are integrated along



the orbit using a Runge-Kutta scheme. The ‘amoeba’ routine of Press *et al.* (1986) is used to refine successive guesses of the initial velocities, subject to the constraint that the component of the velocity of the test particle is consistent with the mean radial velocity in the observed fields presented above.

Since the data are binned, it is natural to use the  $\chi^2$  statistic for this comparison:

$$\chi^2 = \sum_{fields} (v_i - v_{model})^2 / \delta v_i^2, \quad (5)$$

where  $v_i$  is the mean velocity in field  $i$ ,  $\delta v_i$  is the standard error on  $v_i$  and  $v_{model}$  is the projected velocity of the test particle at the point in its orbit that corresponds to the position on the sky of field  $i$ .

The orbit of the test particle which minimizes  $\chi^2$  as defined above, is shown in Figures 10 and 11. The left-hand panel in Figure 10 shows the radial velocity data in the  $b - v$  plane together with the test-particle orbit. This fit is formally acceptable (reduced  $\chi^2 = 1.7$ ), in spite of the systematic differences between the model and the mean velocity data. The curvature of the data near  $b = -15^\circ$  is so extreme that no orbit in the above potential can be made to pass through the data points better than this. The right-hand panel compares the orbit to the heliocentric distance measurements presented in Figure 4. This fit is acceptable (reduced  $\chi^2 = 1.8$ ). Note that the distances to the RR Lyrae stars at low latitude (Alard 1996) discussed above in §2.3.2 are not included; we return to this point in §5.3 below. Figure 11 shows the  $x - z$  shape of the best-fit center-of-mass orbit, integrated for  $10^9$  years. The radial period of this orbit — defined as the time taken from apogalacticon to perigalacticon and back — is 0.76 Gyr.

We note that this orbit requires that the end of Sgr farthest from the Galactic plane is closest to the observer, by an amount of  $\sim 2.5$  kpc per ten degrees along the major axis. This prediction is testable by direct determination of the distance to each end of the Sagittarius dwarf. Perhaps the most precise such determination, given the large numbers of identifiable member stars, will be comparison of the mean apparent magnitude of the RR Lyraes in Sgr at either end of the major axis. A large sample is already available from the DUO RR Lyraes, which are near the Galactic Plane and, thus, the more difficult to detect. Note further that this best-fit orbit gives rise to a proper motion of 2.0mas/yr, towards the Galactic plane, in excellent agreement with the measured value of  $2.1 \pm 0.7$ mas/yr in this direction.

### 3.1. Major Axis Rotation?

The mean velocity at each point along the major axis of the Sagittarius dwarf is made up from the sum of the velocity of a test particle at that place moving in the Galactic potential on the same orbit as the center of mass of the Sagittarius dwarf, together with any contribution from systematic motions associated with the internal dynamics of the Sagittarius dwarf. There are two

possible such systematic motions associated with the Sagittarius dwarf itself — internal streaming and bulk figure tumbling.

The numerical calculations summarized in §4 below show that the effect of Galactic tides on a dwarf spheroidal is to generate flattening, and to orient the dwarf spheroidal such that its major axis is aligned along its orbit, at least near perigalacticon for elliptical orbits. That is, a tidally-distorted dSph galaxy is effectively a bar which is spin-orbit locked near perigalacticon. In this case, no bulk figure tumbling bringing the major axis out of the plane of the orbit is expected. In §2.6 above we placed tight limits on any minor axis rotation. Thus, we restrict discussion here to consideration of any possible internal streaming motions in the Sagittarius dwarf spheroidal involving rotation parallel to the apparent major axis.

Is it plausible that the Sagittarius dwarf spheroidal is a rotating body? Hargreaves *et al.* (1994a) found no significant rotation in the Sextans dSph, but discovered rotation about the long (major) axis of Ursa Minor (Hargreaves *et al.* 1994b). They speculated that the rotation in the latter case was attributable to tidally-induced streaming motions. In any case, the amplitude in UMi is a small fraction of the internal velocity dispersion. Thus, based on the precedent of the other dSphs, no significant internal streaming motion is expected in the Sagittarius dwarf. It is probable that the observed mean velocity is correctly representing that which is appropriate to determine the orbit of Sgr about the Galaxy. Nonetheless, we consider as a limiting case the possibility that the Sagittarius dwarf is flattened entirely by internal streaming, and that streaming is oriented so as to have the maximum possible effect on the observed mean stellar velocities.

The Sagittarius dwarf is significantly flattened, with 3-dimensional shape  $\sim 3:1:1$ . Binney (1978) studied models of self-gravitating (with mass following light) prolate galaxies flattened by internal rotation. We assume (maximally) that the apparent ellipticity of Sgr is the true ellipticity, and that the shape is determined entirely by rotation, with no Galactic tidal contribution. Then Fig 2 in Binney (1978) indicates that, if rotationally flattened with ellipticity  $\epsilon = 1 - a_1/a_3 \sim 0.67$ , that the maximal streaming velocity in the Sagittarius dwarf is approximately equal to its velocity dispersion. For consistency with the model developed below, we further assume that Sgr rotates with a solid body rotation curve about a point near M54. In that case, the maximum rotation velocity corresponds to  $|\Omega_{rot}| \lesssim 1 \text{ km/s/degree}$ . We note that a robust test of this model will be possible by determination of the mean velocity for the DUO RR Lyrae stars, which are at the other end of the major axis of the Sagittarius dwarf than the location of the stars for which we have extant kinematic data.

The orbital calculations described in the previous section were altered to account for such bulk rotation. The radial periods resulting from fits to the data were lengthened to 1.0 Gyr for  $\Omega_{rot} = 1 \text{ km/s/degree}$  (in the sense that lower end of the Sagittarius dwarf spheroidal near Ter 8 is rotating away from the observer) and shortened to 0.6 Gyr for  $\Omega_{rot} = -1 \text{ km/s/degree}$ . Thus, the period of the orbit of the Sagittarius dwarf spheroidal cannot be greater than  $\sim 1.0 \text{ Gyr}$  even

if it is conspiring to rotate in such a way so as to counteract the observed velocity gradient. None of the models with major axis rotation in the range  $-1 \text{ km/s/degree} < \Omega_{rot} < 1 \text{ km/s/degree}$  fits the curvature in the velocity curve near  $b = -15^\circ$  evident in Fig 10.

Thus, the orbital period of the Sagittarius dwarf about the Galaxy has a formal best value of 0.76Gyr. This orbit is formally an acceptable fit to the extant kinematics, in spite of the apparent systematic deviations. No orbit, subject to the assumptions specified above, with period significantly longer than  $\sim 1\text{Gyr}$  provides an acceptable fit to the data. We note here that it is implausible that the Sagittarius dwarf has been recently captured by the Milky Way. For this to have happened, a non-destructive encounter of Sgr with a rather massive companion galaxy is required to perturb its orbit sufficiently. The apocenter we have derived is similar to the current distance of the Large Magellanic Cloud, but the current constraints on the orbit of the LMC (Jones, Klemola & Lin 1994) are not consistent with such a scenario.

#### 4. Results of numerical simulations of the evolution of dwarf spheroidal galaxies

All of the orbits calculated above have periods  $\lesssim 1\text{Gyr}$ , implying more than ten perigalacticon passages over the last 10 Gyr, which is the minimum age of the dominant population in Sgr. Johnston *et al.* (1995) and Velasquez & White (1995) attempted to model the orbital evolution of the Sagittarius dwarf using the IGI-I data as constraints. Analyses of the tidal effects on generic satellite galaxies by Piatek & Pryor (1995) and by Oh, Lin & Aarseth (1995) are also relevant in considering the survival of the Sagittarius dwarf over its lifetime, at least in terms of what did *not* occur.

The conclusions in common in all of these studies are that the dwarf galaxies in which mass follows light lose a very substantial amount of mass at every close perigalacticon passage. The internal velocity dispersion in the satellite does not change significantly prior to disruption (the dispersion may in fact decrease during disruption) and the stellar surface density distribution remains well described by a King model until near total disruption. Thus, there are no clear observational signatures of the tidal disruption of a dSph galaxy, prior to its final demise, except the very obvious one of the presence of a substantial tail of stellar (and dark matter) debris spreading along a dispersion orbit with the remnant dSph galaxy.

Piatek & Pryor (1995) modeled the evolution of a stellar satellite galaxy with parameters similar to those inferred from the luminous component of the Ursa Minor dwarf spheroidal — masses in the range  $3 - 8 \times 10^5 M_\odot$ , no dark matter and with the stars described by a single-component King model, with core radius (defined by them to be the radius at which the surface brightness has fallen by a factor of two) of 140 pc and tidal radius of 643 pc. The orbits investigated in the simulations had perigalacticon at 30 kpc, and various apogalacticon distances, but were always highly elliptical. A range of Galactic potentials was assumed, from the extreme of a point mass to an infinite dark halo. Piatek & Pryor found that, generically, the dwarf spheroidal

is stretched along its orbit and compressed in the perpendicular directions. The amplitude of the tidal effects is very sensitive to perigalactic distance, but only moderately sensitive to the intrinsic mass of the dwarf. In general, the apparent M/L of the dwarf changed only a little before complete disruption of the dwarf spheroidal, which took a very small number, of order one, of perigalactic passages.

Oh, Lin & Aarseth (1995) consider an extensive series of calculations investigating the evolution of fragile systems in tidal fields. They also assumed as initial conditions for the satellite galaxy a single-component, isotropic King profile, with core radius of a few hundred parsecs and, in this case, a mass in the range  $2 - 6 \times 10^6 M_\odot$ . Thus, again they simulated the evolution of a low-density stellar satellite, with no dark matter. In agreement with Piatek & Pryor (1995), they found that the dwarfs were distorted into a triaxial configuration, such that the longest axis is in the direction of the orbit. After a significant fraction of the original mass is lost, the flattening in the orbital plane is preserved, but the major axis becomes skewed, with the leading end closer to the Galaxy and the trailing tail further away. After disruption, the stars which escaped attain Galactic orbits similar to that of the original parent satellite galaxy. When a dwarf spheroidal is tidally disrupted, the velocity dispersion of the unbound, but not-yet-dispersed stars is comparable to that internal to the dSph, in virial equilibrium just prior to the disruption. Thus, an observed large velocity dispersion implies the presence of a large mass, which is dark matter in the case of dSph, irrespective of whether or not the stars are in virial equilibrium or the dSph is being tidally disrupted.

Oh, Lin & Aarseth (1995) show that the rate at which a dSph galaxy is disrupted is a very sensitive function of the ratio of its physical size to its tidal radius (see also Johnston, Hernquist & Bolte (1996) who characterized survivability in terms of density contrast). Dwarf spheroidal galaxies whose initial extent is less than approximately twice their tidal radius are typically able to survive for a Hubble time.

The above two sets of simulations lead to models which include dark matter in the satellite galaxy, to increase its survivability. Velasquez & White (1995) modeled the orbital evolution of the Sgr dwarf, adopting a King model for the dwarf with a mass of  $\sim 10^8 M_\odot$ , a core radius of 527 pc and tidal radius of 2735 pc. They derived a period of order 0.75 Gyr and perigalactic distance of  $\sim 10$  kpc. They found that a single passage through this pericenter completely disrupts the dwarf, unbinding some 95% of its mass within two orbital passes. They emphasize, however, that their orbit requires the Sgr galaxy to survive at least 10 pericentric passages before being almost entirely disrupted on the passage immediately preceding the present one. No mechanism to ensure the survival the Sgr dwarf prior to its current orbit is discussed.

Johnston, Spergel & Hernquist (1995) also modeled the specific case of the Sagittarius dwarf, this time adopting as a model a Plummer sphere (which has a constant density core and  $\rho \propto r^{-5}$  envelope) with a mass of either  $10^7 M_\odot$  or  $10^8 M_\odot$  and a scale radius of 600 pc. They analyzed a variety of orbits with periods in the range 1.5–2.5 Gyr, none of which is, however, consistent with

the observed low gradient in mean radial velocity along the Sgr dwarf. Johnston *et al.* note that fitting the shallow velocity gradient discussed above requires shorter orbital periods and, with their adopted model of the Sagittarius dwarf spheroidal, an unacceptably high disruption rate of the dwarf, in agreement with the conclusions of Velasquez & White (1995). Johnston *et al.* (1995) considered in detail the stability of the dwarf, as a function of orbital parameters. Even with their least disruptive orbits and more massive satellite galaxy, some 20% of the original satellite mass is tidally stripped at each pericentric passage. They confirm that the effect of this mass loss on the current internal kinematics of the dSph is minimal, with the central velocity dispersion and its radial variation, being almost entirely unaffected. Similarly, no perceptable deviations from the original Gaussian velocity profiles are generated.

## 5. Mass Density and Survivability of the Sagittarius dwarf spheroidal

The simulations discussed above obviously did not model the case of the Sagittarius dwarf, since it has persisted for many more orbital periods than any of the dwarfs in those analyses. Their relevance for the case of the Sagittarius dwarf lies in the understanding of the prolate shape of the Sagittarius dwarf spheroidal as reflecting the effects of Galactic tides. We propose below that the Sagittarius dwarf spheroidal is being tidally stretched along its major axis, which is aligned with its orbit, and is presently tidally limited. We present a self-consistent model with these properties.

### 5.1. The Mass Profile of the Sagittarius dwarf spheroidal

The extant simulations of the orbital evolution of the Sagittarius dwarf spheroidal which allowed the presence of dark matter — namely those by Johnston, Spergel & Hernquist (1995; their more massive satellites) and by Velazquez & White (1995) — were limited to ones where the light traced the mass. These simulations concluded that the Sagittarius dwarf spheroidal should be rather easily disrupted, leading to the conundrum of its age being an order of magnitude greater than its predicted lifetime. How can one circumvent these contradictory conclusions? We begin by considering the properties expected of a dark halo in a dwarf galaxy.

Gas-rich dwarf irregular galaxies have HI rotation curves that are rising over much of the extent of the data (*e.g.*, Carignan, Beaulieu & Freeman 1990; Lake, Schommer & van Gorkom 1990), *i.e.*, solid-body rotation curves. This suggests that they are embedded in a dark halo of almost constant density, so that the optical galaxy — and the more-extended HI gas disk — resides within a dark halo whose core radius is significantly larger than the extent of the luminous galaxy. Fits to the rotation curves of gas-rich dwarf galaxies which do have a turn-over in the rotation curve provide values of the dark halo core radius of around 3 kpc (*e.g.*, Lake, Schommer & van Gorkom 1990; Moore 1994). Dwarf irregulars are significantly more dark-matter-dominated than are large spirals (*cf.* Carignan, Beaulieu & Freeman 1990); indeed lower luminosity spirals

may be more dark-matter dominated than are higher luminosity spirals (Persic, Salucci & Stel 1996).

Model-dependent determinations of the density of dark matter in the core of the gas-rich dIrr galaxies discussed above provide rather high values,  $\lesssim 0.1 M_{\odot}/\text{pc}^2$ . As emphasized by Moore (1994), the large core radii for the dark halos around gas-rich dwarf galaxies are not consistent with the halos consisting of Cold Dark Matter. CDM-dominated N-body simulations predict rotation curves which are significantly steeper in the inner regions than those observed, even before taking account of the likely added CDM contraction after baryons settle in the central regions of the dark halo (*cf.* Flores *et al.* 1993). Note that to be trapped at all in such small-scale systems, the dark matter has to be either very cold non-baryonic matter, or dissipative (hence baryonic).

We propose that the gas-poor dwarfs, such as the dSph, have dark halos similar to those of the gas-rich dwarfs. This is of course what one would expect if it is only star formation histories and gas flows that differentiate the two types of galaxy. The close proximity of the dSph to the Milky Way raises the possibility of tidal truncation of the halos of the dSph, leaving the constant density core (provided it is of high enough density). Thus, we consider the situation if the Sagittarius dwarf stars are embedded in a constant-density dark halo. We will retain the usual assumption that the system is isothermal — as discussed above, the observations of the velocity dispersion are quite consistent with no variation across the face of Sgr — and has an isotropic velocity dispersion tensor. Models of this type were analyzed by Lake (1990) and by Pryor & Kormendy (1990) in analyses of the Draco and Ursa Minor dSphs.

## 5.2. The Survival of the Sagittarius dwarf spheroidal

An isothermal tracer population embedded within a constant density (spherical) dark halo (corresponding potential  $\Phi(r) = 2\pi G\rho_0 r^2$ ) will have phase space density

$$f \propto \exp(-E/\sigma^2), \tag{6}$$

where  $E = \Phi + \frac{1}{2}v^2$  and  $\sigma$  is the one-dimensional velocity dispersion. The integral of this expression over velocities gives the volume density of the tracer stars,

$$\rho_*(r) = \rho_*(0) \exp(-\Phi/\sigma^2). \tag{7}$$

Substitution of the expression above for the potential (quadratic in coordinate  $r$ ), defining the characteristic scale  $a$  such that  $a^2 = \sigma^2/2\pi G\rho_0$ , and integration down the line-of-sight yields the observable surface brightness profile, assuming no radial gradient in the conversion from stellar number density to surface brightness, that is, no radial mass segregation:

$$I(R) = I_0 \exp(-R^2/a^2). \tag{8}$$

Thus the surface brightness profile of an isothermal tracer population of given velocity dispersion in a simple harmonic potential (constant density) is a Gaussian in the projected distance from the

center, with a width determined by the value of the constant density. This Gaussian has fallen to half its central value at  $R_{HB} = \sqrt{\ln 2} a = 0.83 a$  and, using the definition of  $a$  above,

$$(G\rho_o)^{-1/2} = \sqrt{\frac{4\pi}{4.16}} \frac{R_{HB}}{\sigma}. \quad (9)$$

As discussed by Lake (1990) and by Pryor & Kormendy (1990), relaxing in this manner the requirement that light traces mass (explicitly required in fits of one-component King models to the light profile) provides a determination of the central mass density which is a factor of  $\gtrsim 2$  lower than the King model value.

Note that, in principle, this model may be tested by this prediction of a Gaussian surface brightness profile; the current data for the Sagittarius dwarf spheroidal are not of high enough S/N for this to be a constraint. As shown by Lake (1990) and by Pryor & Kormendy (1990), the fits to Ursa Minor are acceptable, while some velocity anisotropy seems to be required for Draco — the Gaussian fall-off is too steep. Recall, however, that an initially isothermal velocity distribution function which is truncated by tides is exactly a King model, so that one does not expect a pure Gaussian model to be a good fit to the data, but neither is adequacy of fit by a King model an argument in favor of the assumption that mass traces light.

The minor-axis radius at which the surface brightness of the Sagittarius dwarf spheroidal has fallen by a factor of two was derived above to be  $R_{HB} \sim 550$  pc (but, as discussed, is uncertain due to problems with subtracting Galactic foreground stars over a large range in Galactic latitude), in very good agreement with the independent estimate of the line-of-sight half-width. The line-of-sight stellar profile is the relevant quantity for substitution into equation (9) above (*cf.* Lake 1990). The velocity dispersion of the Sagittarius dwarf spheroidal is well-determined. Thus a reasonable estimate of the central mass density of the Sagittarius dwarf spheroidal is

$$\rho_o = 0.03 (550 \text{ pc}/R_{HB})^2 (\sigma/11.4 \text{ kms}^{-1})^2 M_\odot \text{ pc}^{-3}. \quad (10)$$

The total mass of the Galaxy interior to the present position of the Sagittarius dwarf spheroidal,  $d \sim 15$  kpc, for a flat rotation curve with  $V_c = 220 \text{ km s}^{-1}$  is

$$M(< 15 \text{ kpc}) \sim 2 \times 10^{11} M_\odot, \quad (11)$$

giving a mean enclosed density of

$$\langle \rho \rangle \sim 0.013 M_\odot \text{ pc}^{-3}. \quad (12)$$

Note that the halo density evaluated *at* 15 kpc is

$$\rho_{halo}(15 \text{ kpc}) \sim 0.004 M_\odot \text{ pc}^{-3}. \quad (13)$$

Thus the density inferred for the Sagittarius dwarf spheroidal on the basis of a constant-density dark halo model is  $\sim 3$  times greater than the mean background density interior to pericenter.

The number of orbits that a satellite can remain intact against a background tidal field increases with the density contrast between the satellite and the mean background density interior to pericenter of its orbit. Indeed, the classical Jacobi/Roche criterion — which assumes point masses, circular orbits and phase-locking of the satellite in its orbit — gives that a factor of three in mean density contrast between the satellite and the main galaxy is required for stability of the satellite. Note that the classical tidal radius derived using the Jacobi integral is a remarkably good approximation in many cases, but recall the result from Oh, Lin & Aarseth that satellites on elliptical orbits could persist provided their limiting radius was less than *twice* their tidal radius at perigalacticon. Satellites on elongated orbits are expected to be more robust, for a given pericenter (*cf.* Allen & Richstone 1988). Johnston, Hernquist & Bolte (1996) recently investigated the evolution of satellites in strong tides and characterized their longevity by the ratio of central density of the satellite to the mean background. However, the mean density of the satellite is the more meaningful quantity for such a comparison. The Plummer model profiles adopted by Johnston, Hernquist and Bolte have a mean density within two scale-lengths (close to the outer detectability limit) a factor of  $\sim 8$  below the central density and, hence, a factor of 8 below the mean density of a uniform system, as modeled here. They found that a central density of the satellite which is a factor of 30 higher than the mean background interior to perigalacticon was sufficient for a satellite to survive. This translates into a density contrast of  $\sim 3$  as being the requirement for a tidally robust, uniform density satellite, as discussed here, in remarkable agreement with the Roche criterion.

These results imply that the structure we propose for the Sagittarius dwarf is fairly robust, and also that tides have peeled away the outer, lower density envelope to the halo (otherwise the factor of three is a mere coincidence). The Sagittarius dwarf spheroidal is not impervious to Galactic tides, and is being tidally limited and distorted, though not disrupted.

With the model of a constant-density dark halo, estimation of the total mass of the Sagittarius dwarf spheroidal is straightforward, providing one can argue for a cutoff radius. The tidal limitation suggests that one be guided by the extent of the stars down the minor axis. Self-consistency of our picture also requires that the mass be low enough that dynamical friction be ignorable.

The fits to gas-rich dwarfs discussed above found a core radius for the dark halos of  $\sim 3$  kpc. The minor axis extent of the stellar component of the Sagittarius dwarf spheroidal is  $\sim 1.7$  kpc, and is a lower limit to the possible extent of the dark halo in this direction. We shall adopt 2 kpc as a fiducial for the cut-off radius of the constant-density dark halo,  $R_{Sgr,halo}$ ; one should be aware of the dependencies of derived quantities on this value (we express all quantities with this dependence explicitly).

$$M_{Sgr,halo} \sim \frac{4\pi}{3} R_{Sgr,halo}^3 \rho_o, \quad (14)$$

$$M_{Sgr,halo} \sim 10^9 M_\odot (R_{Sgr,halo}/2\text{kpc})^3 (\rho_o/0.03 M_\odot \text{pc}^{-3}). \quad (15)$$



The mean orbital Galactocentric distance derived above is  $\sim 30$  kpc, thus

$$t_{dyn\ fric} \sim 1.3 \times 10^{10} \text{ yr} \left( \frac{d}{30 \text{ kpc}} \right)^2 \left( \frac{10^9 M_\odot}{M_{Sgr}} \right). \quad (16)$$

Detailed numerical simulations are required to test the conclusions about tidal stability and orbital evolution based on these analytic approximations.

### 5.3. Consistency of the Model with the Derived Orbit

In §3 we derived the orbit of the Sagittarius dwarf under the assumption that the internal binding force was negligible. This assumption is, of course, at odds with the model presented above, which proposes the existence of a dense dark matter halo around the dwarf to ensure its survival against Galactic tides until the present time. Below, we therefore investigate the projected distance and projected velocity of the stellar component of the Sagittarius dwarf in the presence of the proposed dark matter halo, to check whether the assumptions used in §3 to calculate the orbit of the center of mass of the Sagittarius dwarf still hold to a reasonable approximation.

In the model presented in §5.2 above, the internal dynamics of the Sagittarius dwarf are completely dominated by a dark-matter halo, which, for simplicity, is assumed to be spherical. As the nature of dark matter remains unknown, the simplest assumption is that the dark matter mass distribution does not vary significantly with time. This means that the self-gravity of the stellar component is negligible, so the orbits of tracer stars in the dark matter halo can be integrated without the need to resort to an N-body scheme.

A spherical isothermal population of 10000 particles was constructed according to Eqns 6 and 7, and was placed in a dark halo of constant-density  $\rho_0 = 0.03 M_\odot \text{ pc}^{-3}$  and radius 1.4 kpc. The center of mass of the dark matter halo will follow some orbit in the Milky Way potential; for concreteness, suppose it moves along the orbit calculated in §3. At a given time  $t$ , a tracer-particle of the stellar population will find itself at a distance  $d$  from the center of mass of the Sgr dark halo. So in addition to the acceleration due to the Galactic mass distribution (the assumed potentials are given in §3), the particles experience an acceleration  $a_{Sgr} = G \frac{4}{3} \pi \rho_0 d$  if  $d < 1400 \text{ pc}$  or  $a_{Sgr} = GM_{Sgr}/d^2$  if  $d > 1400 \text{ pc}$ . The numerical method used to integrate the orbits was identical to that described in §3.

The integration was started 10 Gyr ago, and evolved up to the present — fully 12 orbits — at which time the radial velocity gradient and distance were projected onto the line of sight from the Sun. Figure 12 compares the radial velocity gradient and the heliocentric distances of the stellar tracer particles in this model, with those based on the orbit of the center of mass orbit. Both techniques give predictions that are consistent with the observations, and in particular inclusion of the internal forces produce stellar distances across the face of the Sagittarius dwarf that may be in better agreement with the RR Lyrae distances at low latitudes, but the uncertainties in those

data are large.

The above simulation is presented solely as a crude consistency check of the proposed model. An obvious problem with this approach is that the model does not extend far enough along the major axis to test the velocity observations well away from the photometric center of the Sagittarius dwarf; this is because the simple analytical model constructed in §5.2 is spherical, fit to the minor axis profile, while the kinematic and distance information are fit along the major axis.

#### 5.4. Dynamical Implications for the Milky Way Galaxy

Only the *central* density of the background dark halo of the Milky Way (Merrifield 1992) equals the mean density that we have calculated for the Sagittarius dwarf spheroidal, so it is not likely that the Sagittarius dwarf spheroidal will be tidally shredded by the Galactic halo acting alone; the disk contributes an important part of the potential (but the structure of the disk is unimportant, see also Velasquez & White 1995). The mean density of the Sagittarius dwarf spheroidal obtained above is perhaps 10 times that of the disk at 15 kpc — Kuijken & Gilmore (1989) find that the disk has density  $\rho_{disk}(15 \text{ kpc}) \sim 8 \times 10^{-3} M_{\odot} \text{ pc}^{-3}$ , while the heavier disk modeled by Velasquez & White (1995), which has a total surface density at the solar neighborhood of  $72.6 M_{\odot} \text{ pc}^{-2}$ , has twice this,  $\rho_{disk}(15 \text{ kpc}) \sim 0.014 M_{\odot} \text{ pc}^{-3}$ . The relatively high density of the Sagittarius dwarf spheroidal raises the possibility that the Sagittarius dwarf spheroidal could indeed impart some damage to the Milky Way as it is accreted, if it could couple to the disk.

Following Ostriker (1990), the absolute maximum amount of energy that could be imparted to the disk is the total orbital energy of the satellite, giving an increase of random energy of disk stars of

$$\Delta v^2 \sim v_{orbit}^2 M_{Sgr} / M_{disk}, \quad (17)$$

which is

$$\Delta v^2 \sim 250^2 \times 10^{-2} (M_{Sgr} / 10^9) (5 \times 10^{10} / M_{disk}) \sim (45 \text{ km/s})^2. \quad (18)$$

If *all* of this energy could be put into vertical heating, and the initial disk has  $\sigma_z \sim 20 \text{ km/s}$  dispersion, this would be increased to  $\sim 50 \text{ km/s}$ . Of course this is a highly unlikely event — the energy absorbed by the disk would be spread among its internal degrees of freedom, even neglecting the internal degrees of freedom of the satellite, and of the dark halo and the dissipation of gas. Binney (1992) has reviewed the role that accretion may play in the generation and sustaining of warps in disks. The mass that we have derived for the Sagittarius dwarf spheroidal is sufficiently high to suggest a role in the generation of the Milky Way warp, as suggested by Lin *et al.* (1996).

## 6. The Properties of the Sagittarius dwarf spheroidal

### 6.1. The Mass/Luminosity Ratio of the Sagittarius dwarf spheroidal

The volume mass density we have derived above may be transformed into a surface mass density using our adopted shape for the Sagittarius dwarf spheroidal, as:

$$\Sigma \sim \rho \times 2R_{halo, Sgr} \sim 0.03 \times 2 \times 2 \times 10^3 M_{\odot} \text{ pc}^{-2} \sim 150 M_{\odot} \text{ pc}^{-2}. \quad (19)$$

Mateo *et al.* (1995a) estimate that the central surface brightness of the Sagittarius dwarf spheroidal is  $\sim \mu_V \sim 25.4$  mag/square arcsec, which corresponds to  $\sim 3L_{\odot} \text{ pc}^{-2}$ . Thus an estimate of the central  $M/L_V$  of the Sagittarius dwarf spheroidal is  $\Sigma/\mu_V \sim 50$ .

The Gaussian star-count profile derived above contains a total luminosity

$$L_V = \pi I_0 a^2 \sim 3.4 \times 10^6 L_{V\odot} \quad (20)$$

with the parameter values obtained earlier. Adopting all of the parameter values from the same model fit implies a global  $(M/L)_V \sim 300$ . However, model-independent estimates of the total luminosity of the Sagittarius dwarf suggest  $L_V \gtrsim 10^7 L_{V\odot}$ , giving a global  $(M/L)_V \sim 100$ .

Previous determinations of M/L ratios for dSph (*e.g.*, Hargreaves, Gilmore, Irwin & Carter 1994) have generally used King model fits and the expression

$$\frac{\rho_o}{\mathcal{L}_o} = \eta \frac{333\sigma_o^2}{R_{HB}I_o}, \quad (21)$$

for the central M/L ratio in solar units, where  $\mathcal{L}$  is the luminosity density and  $\eta$  is a parameter close to unity whose value depends on the King model fit. This expression gives

$$\frac{\rho_o}{\mathcal{L}_{o,V}} = \eta 22.2, \quad (22)$$

in reasonable agreement with the value obtained above.

### 6.2. Dwarf Spheroidal Masses and Chemical Evolution

The model proposed above results in a central  $M/L_V$  for the Sagittarius dwarf spheroidal of around 50 in solar units. Irrespective of any detailed modeling, the high stellar velocity dispersion,  $\sim 11 \text{ km s}^{-1}$ , and the low central surface brightness noted above, provide incontrovertible evidence that the Sagittarius dwarf spheroidal has a high central mass to light ratio. Thus the Sagittarius dwarf spheroidal joins the ranks of those dSph for which there is strong evidence for substantial amounts of dark matter, namely Draco, Ursa Minor, Sextans, Carina and Leo II. The most recent estimates of central mass-to-light ratios are discussed by Irwin & Hatzidimitriou (1995), presented in their Table 10. Fornax, Leo I and Sculptor have derived M/L values which remain (marginally) consistent with a normal stellar population.

Correlations between M/L and other properties of the dSph potentially constrain the nature of the dark matter, though in a manner which has yet to be clarified. The then-extant inverse correlations between M/L and luminosity, and M/L and mean [Fe/H], were interpreted by Dekel & Silk (1986) as supporting CDM dark halos, and by Larson (1987) as indicative of IMF variations and baryonic halos. In any case, the Sagittarius dwarf spheroidal provides a striking counter-example to these correlations.

Lee (1995) has recently presented the available metallicity — surface-brightness and metallicity — luminosity data for dwarf galaxies in the Local Group (his Figure 9). If the Sagittarius dwarf spheroidal were to lie on the relations for dSphs, then with a metallicity of  $\sim -1$  dex, it would be expected to have a luminosity  $M_V \sim -16$ , or  $L_V \sim 2 \times 10^8 L_\odot$ , and a central surface brightness in the V-band of  $\gtrsim 20$  mag/square arcsec. The luminosity estimated from the number of horizontal branch stars within the contours of IGI-I is  $M_V = -13$ , and the central surface brightness is 25.4 mag/square arcsec. The Sagittarius dwarf thus lies 3 mag off the luminosity relation, and 5.5 magnitudes off the surface-brightness relation.

The considerable spread in both the age distribution and the metallicity of the stars in the Sagittarius dwarf, and especially of the globular clusters, constrain the star formation history, and the chemical evolution. While it remains possible in principle that Sgr accreted metal-enriched gas repeatedly during its evolution, the simplest interpretation is that the Sagittarius dwarf spheroidal managed to recycle gas through successive generations of stars, but deciding whether this was by retention of chemically-enriched gas, by re-capture of gas after a supernovae-driven wind (*cf.* Silk, Wyse & Shields 1987) or by some other process, requires detailed age and chemical element ratio distributions. Retention of gas would suggest either that Sgr is/was a fairly massive galaxy, with a large enough escape velocity, or that there was always a low star-formation rate, since the combination of high star-formation rate and low escape velocity would most probably lead to a wind (*e.g.*, Larson 1974; Wyse & Silk 1985; Dekel & Silk 1986).

Element ratio data will provide unique constraints on the star-formation history and gas flows; a system which forms stars in bursts separated by a hiatus, and retains gas, will enrich the gas in iron from Type Ia supernovae between bursts (Gilmore & Wyse 1991), allowing stars with very low oxygen-to-iron ratios to form in the subsequent burst. By contrast, gas accreted from the inter-stellar medium of the proto-Milky Way, or gas ‘lost’ in a temporary wind from Sgr and re-accreted, mixed with extra Galactic gas, should have the high oxygen-to-iron ratio evident in Galactic field halo stars of the age of the Sgr clusters.

The escape velocity from the Sagittarius dwarf spheroidal is the relevant quantity for winds and chemical evolution considerations and may be evaluated with the present model for the structure of the Sagittarius dwarf spheroidal. An homogeneous sphere, truncated at  $r = a$ , has an escape velocity from  $r < a$  of:

$$\frac{1}{2}v_e^2 = 2\pi G\rho(a^2 - \frac{1}{3}r^2). \quad (23)$$

For  $a = 1.2$  kpc, this gives  $v_e(r = 0) \sim 90$  km/s. This value is sufficiently high that the Sagittarius

dwarf spheroidal may be expected to retain a substantial mass of gas, even while forming stars fairly actively.

For comparison, the escape velocity from a self-gravitating system with power-law density profile  $\rho(r) \propto r^{-\alpha}$ ;  $2 < \alpha < 3$  is  $v_{esc} = \sqrt{2} v_{circ} / \sqrt{(\alpha - 2)}$ , where  $v_{circ}$  is the circular velocity parameterizing the gravitational potential. Assuming approximately isothermal velocity dispersions,  $v_{circ} \approx \sqrt{\alpha} \sigma_{1-D}$ , with  $\sigma_{1-D}$  the observed central stellar velocity dispersion. Thus, for a system with power-law density profile exponent  $\sim 3$ , and  $\sigma = 10$  km/s, the escape velocity is  $v_{esc} \approx \sqrt{6} \cdot \sigma_{1-D} \approx 25 \text{ km s}^{-1}$ .

Thus, while this is at best a partial explanation, a constant-density mass profile of the form adopted here does reduce somewhat the discrepancy between calculated escape velocities from stellar systems which evidently were able to form chemically-enriched stars, and that escape velocity required to prevent supernova-driven winds, which would prevent later generations of stars from being formed.

## 7. Summary

We present a self-consistent picture of the structure of the Sagittarius dwarf spheroidal, the nearest satellite galaxy to the Milky Way. We combine extant data on its distance, metallicity, age and stellar populations with new photometric and spectroscopic data which determine its size, shape and dynamics.

The geometrical picture derived from these data is that the Sagittarius dwarf is a prolate body with axis ratios  $\sim 3:1:1$ . The center of Sgr is  $\sim 25$  kpc from the Sun and  $16 \pm 2$  kpc from the Galactic center. The Sagittarius dwarf spheroidal is oriented approximately perpendicular to the plane of the Galaxy from Galactic latitude  $b = -4^\circ$  to  $b = -26^\circ$ . Its longest dimension extends  $\gtrsim 9$  kpc along the coordinate line  $l = 5^\circ$ . The Sagittarius dwarf spheroidal contains a mix of stellar populations ranging from relatively old stars — many RR Lyrae stars are observed and at least one of its four globular clusters is as old as the oldest Galactic halo clusters — to intermediate age stars — several Carbon stars have been identified. The dominant population however, is 10 to 14 Gyr old and has corresponding mean abundances between  $[\text{Fe}/\text{H}] = -0.8$  and  $[\text{Fe}/\text{H}] = -1.2$ . The full abundance range observed covers  $\gtrsim 1$  dex around this mean.

The kinematic data presented include a first study of the proper motion of Sgr, together with intermediate ( $\sim 12 \text{ km s}^{-1}$ ) and high ( $\sim 2.5 \text{ km s}^{-1}$ ) accuracy radial velocity measurements of its member stars. Due to a lack of known extra-galactic reference objects in these low Galactic latitude fields, the proper motion was measured with respect to Galactic foreground stars. This approach means that only the motion in the direction perpendicular to the plane of the Galactic disk is constrained; this component of its velocity is  $250 \pm 90 \text{ km s}^{-1}$ , directed towards the Galactic Plane.

The radial velocity data determine the kinematics at several positions along the major axis from  $b = -26^\circ$  to  $b = -12.5^\circ$ . These data show that the Sagittarius dwarf has an internal velocity dispersion, of  $11.4 \pm 0.7 \text{ km s}^{-1}$ , which is formally consistent with being constant over the face of the galaxy. The mean velocity gradient  $dv/db$  is small in the central regions but the amplitude increases to  $dv/db = -3 \text{ km/s/degree}$  over the outermost three degrees for which we have data.

These kinematic data indicate that Sgr has no significant rotation about its minor axis, but they do not constrain the rotation about its major axis, due a lack of sampling in the latitude range  $b > -12.5^\circ$ . This uncertainty in the major axis rotation rate is a source of uncertainty in the determination of the orbit of Sgr. However, for all plausible internal rotation rates the orbital period is  $\lesssim 1 \text{ Gyr}$  and the perigalactic distance is  $\sim 12 \text{ kpc}$ . This orbital period is much shorter, by about a factor of  $\gtrsim 10$ , than the age of the bulk of its stellar population. We argue that dynamical friction will not have induced significant orbital decay, and that it is unlikely that the Sagittarius dwarf spheroidal has been captured recently, so it has apparently survived many perigalacticon passages.

Given these observational constraints, the consistency of models of Sgr is explored in the context of recent results from numerical simulations of disrupting satellite galaxies. Perhaps the most restrictive result from these simulations is that tidally disrupted debris retains the velocity dispersion of its progenitor. Thus, the measured velocity dispersion is a clear indication that the Sagittarius dwarf spheroidal did not have a much more massive progenitor. Furthermore, if it had been significantly more massive in the past, we would expect to find its ‘missing mass’ as a substantial population of Sagittarius dwarf debris — globular clusters and stars — along its dispersion orbit; however, this is not observed.

The most conservative assumption is to adopt a mass distribution that follows the distribution of luminous matter. The Sagittarius dwarf spheroidal would then approximate a King-model; yet King-models that satisfy the radial light distribution and central velocity dispersion lead to substantial mass loss at each perigalacticon passage (Velazquez & White, 1995; Johnston *et al.* 1995), inconsistent with survival until the present time. This simple mass-follows-light model has too low a mass density at the photometric edge to inhibit tidal dissolution over  $\sim 10$  perigalacticon passages. Sagittarius and, by implication, other dwarf spheroidal galaxies cannot have a mass distribution in which the dark matter profile is similar to that of the luminosity.

We therefore investigate the next simplest model: one that minimizes the total mass required for survival. Such a model has a mass distribution with a large core radius (as is observed in gas-rich dwarf galaxies), so that the mass density is approximately constant over the dwarf. Consequently, the mass to light ratio increases radially outwards from the center of Sgr. This model yields a total  $M/L \sim 100$  and a total mass of  $\sim 10^9 M_\odot$ . This model is consistent with only a small amount of previous tidal dissolution — so the Sagittarius dwarf spheroidal can survive until the present day, is consistent with the observed central velocity dispersion and implies that its orbit has not decayed significantly over its lifetime.

An additional feature of this model is that the escape velocity from the center of the potential well is significantly higher than it is in a power-law model. This reduces to some extent a difficulty with standard models of the chemical evolution of dSph galaxies, that winds generated by star formation and chemical enrichment should remove their gas, preventing chemical self-enrichment.

Contrary to previous estimations, this model suggests that the Sagittarius dwarf spheroidal will resist tidal disruption by the Milky Way and remain an internally bound satellite galaxy until dynamical friction significantly reduces its perigalactic distance, on a timescale of a Hubble time. The robustness of the Sagittarius dwarf spheroidal is consistent with other determinations of the contribution of disrupted dSph to the field stellar halo, which have found this to be  $\sim 10\%$  (*e.g.*, Unavane, Wyse & Gilmore 1996).

Our collaboration was supported by the NSF (INT-9113306) and by NATO. RAI expresses gratitude to the Killam Foundation (Canada) and to the Fullam Award for support. RFGW acknowledges the Seaver Foundation, and thanks Jay Gallagher for many discussions about dwarf galaxies. The Center for Particle Astrophysics is funded by the NSF.

## REFERENCES

- Allen, A. and Richstone, D. 1988, *ApJ*, 325, 583
- Alard, C. 1996, *ApJ*, 458, L17
- Beauchamp, D., Hardy, E., Suntzeff, N.B and Zinn, R. 1995, *AJ*, 109, 1628
- Binney, J. 1978, *MNRAS*, 183, 501
- Binney, J. 1992, *ARA&A*, 30, 51
- Binney, J. and Tremaine, S., 1987 ‘Galactic Dynamics’ (Princeton University Press, Princeton)
- Buonanno, C., Corsi, C.E., Fusi-Pecchi, F., Hardy, E. and Zinn, R. 1985, *A&A*, 152, 65
- Buonanno, C., Corsi, C.E., Fusi-Pecchi, F., Richer, H.B. and Fahlman, G.G. 1995a, *AJ*, 109, 650
- Buonanno, C., Corsi, C.E., Pulone, L., Fusi-Pecchi, F., Richer, H.B. and Fahlman, G.G. 1995b, *AJ*, 109, 663
- Carignan, C., Beaulieu, S. and Freeman, K. 1990, *AJ*, 99, 178
- Carney, B.W., Storm, J. and Jones, R.V. 1992, *ApJ*, 386, 663
- da Costa, G., and Armandroff, T. 1995, *AJ*, 109, 2533
- Chaboyer, B., Demarque, P. and Sarajedini, A. 1996, *ApJ*, 459, 558
- Chiosi, C., Bertelli, G. and Bressan, A. 1992, *ARA&A*, 30, 235
- Dekel, A. and Silk, J. 1986, *ApJ*, 303, 39
- Faber, S. and Lin, D. 1983, *ApJ*, 266, L17
- Fahlman, G., Mandushev, G., Richer, H., Thompson, I., and Sivaramakrishnan, A. 1996, *ApJ*, 459L, 65
- Ferraro, I., Ferraro, F.R., Fusi Pecci, F., Corsi, C.E. and Buonanno, R. 1995, *MNRAS*, 275, 1057
- Flores, R., Primack, J., Blumenthal, G. and Faber, S. 1993, *ApJ*, 412, 443
- Gilmore, G. and Wyse, R.F.G. 1991, *ApJ*, 367, L55
- Hargreaves, J., Gilmore, G., Irwin, M. and Carter, D. 1994a, *MNRAS*, 269, 957
- Hargreaves, J., Gilmore, G., Irwin, M. and Carter, D. 1994b, *MNRAS*, 271, 693
- Hernquist, L. 1990, *ApJ*, 356, 359
- Ibata, R., Gilmore, G., and Irwin, M. 1994, *Nature*, 370, 194.
- Ibata, R., Gilmore, G., and Irwin, M. 1995, *MNRAS*, 277, 781
- Ibata, R. and Gilmore, G. 1995a, *MNRAS*, 275, 591
- Ibata, R. and Gilmore, G. 1995b, *MNRAS*, 275, 605
- Irwin, M. and Hatzidimitriou, D., 1995, *MNRAS*, 277, 1354
- Johnston, K. V., Spergel, D. N., and Hernquist, L. 1995, *ApJ*, 451, 598



- Johnston, K. V., Hernquist, L. and Bolte, M. 1996, preprint
- Jones, B., Klemola, A. and Lin, D., 1994, AJ, 107, 1333
- Kibblewhite, E., Bridgeland, M., Bunclark, P. and Irwin, M. 1984, in  
Proc. Astron. Microdensitometry Conf. NASA-2317 (NASA, Washington DC) p277
- Kuijken, K. and Gilmore, G. 1989, MNRAS, 239, 605
- Lake, G. 1990, MNRAS, 244, 701
- Lake, G., Schommer, R. and van Gorkom, J. 1990, AJ, 99, 547
- Larson, R.B. 1974, MNRAS, 169, 229
- Larson, R.B., 1987, in ‘13th Texas Symposium on Relativistic Astrophysics’, ed. M. P. Ulmer  
(World Scientific, Singapore) p426
- Lee, Y.W., Demarque, P. and Zinn, R. 1994, ApJ, 423, 248
- Lee, M.G., 1995, AJ, 110, 1129
- Lin, D., Richer, H., Ibata, R. and Suntzeff, N. 1996, preprint
- Mateo M., Udalski A., Szymanski M., Kaluzny J., Kubiak M. and Kreminski W. 1995a, AJ, 109,  
588
- Mateo M., Kubiak M., Szymanski M., Kaluzny J., Kreminski W. and Udalski A. 1995b, AJ, 110,  
1141
- Mateo, M., Mirabal, N., Udalski, A., Szymanski, M., Kaluzny, J., Kubiak, M., Kreminski, W. and  
Stanek, K. 1996, ApJ, 458, L13
- Merrifield, M. 1992, AJ, 103, 1552
- Miyamoto, M. and Nagai, R. 1975, PASJ, 27, 533
- Moore, B. 1994, Nature, 370, 629
- Oh, K.S., Lin, D.N. and Aarseth, S.J. 1995, ApJ, 442, 142
- Olszewski, E.W., Schommer, R.A. and Aaronson, M. 1987, AJ, 93, 565
- Ostriker, J.P. in ‘Evolution of the Universe of Galaxies’, ed R.G. Kron, A.S.P. Conf. Series 10,  
(A.S.P., San Francisco, 1990) p25
- Persic, M., Salucci, P. and Stel, F. 1996, MNRAS in press
- Piatek, S. and Pryor, C. 1995, AJ, 109, 1071
- Press, W., Flannery, B., Teukolsky, S. and Vetterling, W. 1986 ‘Numerical Recipes’ (Cambridge  
Univ Press, Cambridge)
- Pryor, C. and Kormendy, J. 1990, AJ, 100, 127
- Richer, H., Harris, W.E., Fahlman, G.G., Bell, R.A., Bond, H.E., Hesser, J.E., Holland, S., Pryor,  
C., Stetson, P.B., Vandenberg, D.A. and van den Bergh, S. 1996, ApJ, 463, 602

- Sandage, A., 1965, in ‘The Structure and Evolution of Galaxies’, ed. H. Bondi (New York, Interscience) p83
- Sarajedini, A. 1993, AJ, 105, 2172
- Sarajedini, A. and Layden, A. 1995, AJ, 109, 1089.
- Sarajedini, A. and Layden, A. 1996 in Formation of the Galactic Halo, ASP Conference Series, Vol. 92, Heather Morrison and Ata Sarajedini, eds., p. 297
- Silk, J., Wyse, R.F.G. and Shields, G. 1987, ApJ, 322, L59
- Suntzeff, N., Kinman, T. and Kraft, R. 1991, ApJ, 367, 528
- Suntzeff, N., Mateo, M., Terndrup, D., Olszewski, E., Geisler, D. and Weller, W. 1993, ApJ, 418, 208
- Unavane, M., Wyse, R.F.G, and Gilmore, G. 1996, MNRAS, 278, 727
- Velazquez, H. and White, S. 1995, MNRAS, 275, L23
- Wyse, R.F.G. and Silk, J. 1985, ApJ, 296, L1

Fig. 1.— Isopleth contours of the tip of the Sgr main sequence, derived from APM measurements of UKST survey plates to the East of the center of Sgr, are shown superimposed on the discovery isopleth map of the red clump stars from IGI 1994. The positions of the globular clusters potentially associated with the Sgr dwarf: M54, Ter 7, Ter 8, and Arp 2 are also indicated, as is the position of the foreground globular cluster M55. Contours for the Sgr main sequence tip start at  $\approx 1$  arcmin $^{-2}$  and increment by  $\approx 5$  arcmin $^{-2}$ .

Fig. 2.— The magnitude distribution of stars in the color strip  $1.05 < V - I < 1.17$  in a field near the center of the Sagittarius dwarf spheroidal (the data are from the comparison field of Sarajedini & Layden 1995). The narrow local maximum at  $V = 18.25$  corresponds to the red clump population in the Sagittarius dwarf spheroidal. The fitted model described in the text is superimposed.

Fig. 3.— The color-magnitude diagram of a  $7' \times 7'$  field at  $(\ell = 15.48^\circ, b = -15.09^\circ)$ , close to the center of the Sagittarius dwarf. Galactic disk dwarfs predominate in the blue vertical feature at  $V - I \sim 0.8$ ,  $V < 17.5$ , while Galactic bulge subgiants predominate in the intermediate color vertical feature at  $V - I \sim 1.1$ ,  $V < 17.5$ . The tip of the Sagittarius dwarf main sequence is seen near  $V - I \sim 0.6$ ,  $V \sim 21$ , while its red clump is at  $V - I = 1.1$ ,  $V = 18$ . The sloping feature from  $V - I = 1.3$ ,  $V = 18$  to  $V - I = 1.5$ ,  $V = 16$  is the RGB of the Sagittarius dwarf spheroidal.

Fig. 4.— The heliocentric distance to 26 fields along a portion of the major axis of the Sagittarius dwarf is shown as a function of Galactic latitude. As described in the text, a correction for the variation in extinction was applied to the photometry, and distances were derived from the fitted  $V$  magnitude of the red clump in each field. The dotted line is a  $\chi^2$  fit to these data (reduced  $\chi^2 = 1.17$ ).

Fig. 5.— The stars whose radial velocity measurements confirm that they are members of the Sagittarius dwarf spheroidal are plotted onto the isopleths presented in Figure 1. The plusses represent the high precision CTIO measurements, while the filled circles correspond to the AAT measurements. A grid of Galactic coordinates has been superimposed.

Fig. 6.— Radial velocities for stars which are members of the Sagittarius dwarf, corrected for the Galactic rotation of the Local Standard of Rest, plotted as a function of Galactic latitude. The velocities of the four globular clusters of the Sgr system are indicated, with the latitude of the globular cluster being at the center of the relevant marker.

Fig. 7.— The velocity data are subdivided into the fields shown in the central panel. For convenience, the isopleth map of the Sagittarius dwarf derived by IGI-I and Galactic coordinate lines have been superimposed. The CTIO velocity data for fields (from left to right) f1, f5, f6 and f7 are displayed in the form of histograms on the top row of this diagram, while the AAT data in all eight fields are displayed on the bottom two rows of the diagram. In all of the histograms displayed on this page, the horizontal coordinate is a Galactocentric radial velocity in km/s and the vertical axis is the number of stars per bin. A fitted Gaussian to each of these data sets has been overlaid and the fitted mean (and dispersion for the CTIO data) is indicated.

Fig. 8.— The run of mean Galactocentric radial velocity along the major axis of the Sagittarius dwarf spheroidal (assumed to be parallel to a line of constant Galactic longitude) is shown in the left hand panel. The right hand panel presents the velocity dispersion profile along the major axis.

Fig. 9.— Limits on minor axis rotation in the Sagittarius dwarf. The three panels show different Galactic latitude slices through the velocity data presented in Tables 2.A, 2.B and Ibata & Gilmore (1995a), their Table B1. Straight-line fits provide no evidence for a gradient in velocity as a function of Galactic longitude in these three fields. The adopted major axis is aligned with the Galactic coordinate line  $\ell = 5^\circ$ .

Fig. 10.— The orbit of a test particle which best fits the kinematic data of the Sagittarius dwarf in the Milky Way potential described in the text is shown projected on the available data. The left hand panel shows the projected velocity of the orbit along the lines of sight to the fields which determine the fit. Formally, this orbit is an acceptable description of the data, despite the systematic difference between the model and the data. The right hand panel compares the heliocentric distance of the guiding center of the orbit fit to the velocity data to the heliocentric distance data presented in Figure 4. The modeled orbit is an acceptable fit to these distance constraints (reduced  $\chi^2 = 1.8$ ).

Fig. 11.— The orbit of the Sagittarius dwarf, integrated over 1 Gyr, is shown in the  $x - z$  plane. The ‘star’ symbol represents the present position of the Sun, while the open ellipse (drawn to scale) gives the present position of the Sagittarius dwarf spheroidal. The radial period of this orbit is 0.76 Gyr.

Fig. 12.— The assumptions used in §3 to derive the orbit of the Sagittarius dwarf are checked for consistency against the analytical model (given in §5.2), which proposes that the mass distribution of the Sagittarius dwarf is dominated by a spherical dark matter (DM) halo. The solid lines show (on the left-hand panel) the radial velocity and (on the right-hand panel) the heliocentric distance along the orbit of the center of mass (derived in §3). The stellar component of the Sagittarius dwarf is modeled as an isothermal population of  $10^4$  non-interacting tracer particles which move under the influence of the (fixed) Galactic potential plus the potential of the Sgr DM halo (which is assumed to move on the orbit of the center of mass). The model is integrated for 10 Gyr and stopped at the present position of the Sagittarius dwarf. The tracer particles are then binned along the major axis in groups of 200; the mean projected radial velocity in these bins is plotted (dots) in the left-hand panel, while mean heliocentric distance is plotted in the right-hand panel, both quantities as a function of Galactic latitude. Since the projected radial velocity and distance profiles to the modeled stellar component are approximately equal to the radial velocity and distance along the orbit of the center of mass, the assumptions stated in §3 hold.

TABLE 1. Physical parameters of the globular clusters of the Sagittarius dwarf spheroidal.

TABLE 2.A. Radial velocity data from 1994 AAT run.

TABLE 2.B. Radial velocity data from 1994 CTIO run.

TABLE 3. Mean velocities and velocity dispersions in the observed fields.

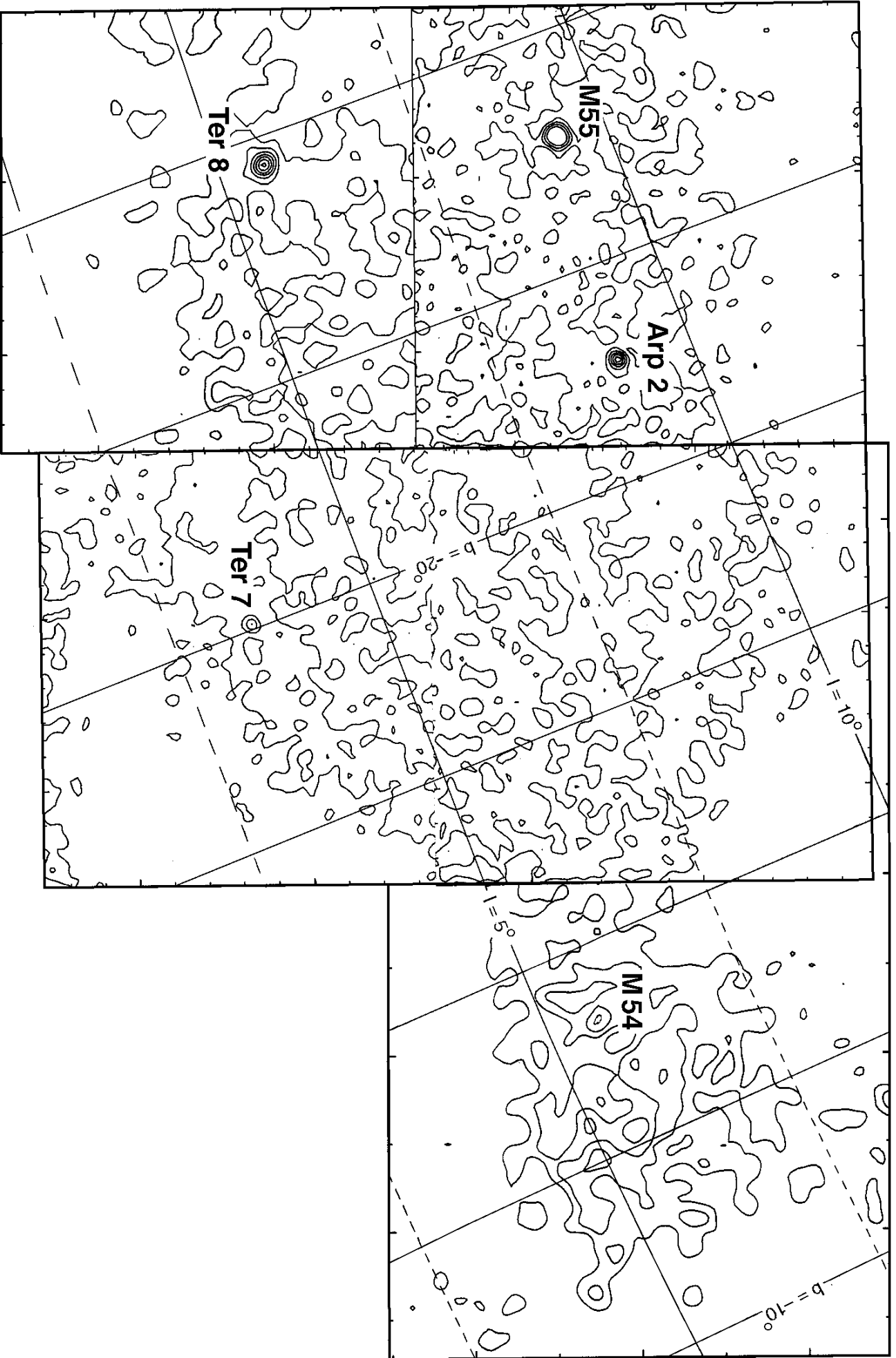


TABLE 1. The globular clusters of the Sagittarius dwarf spheroidal

Cluster	ra (1950)	dec (1950)	[Fe/H]	$v_{Gal}$ (km/s)	$T$ (Gyr)	$M_V$
M54	18 51 51.2	-30 32 34	$-1.55 \pm 0.10$	$172 \pm 1$		-10.0
Ter 7	19 14 26.2	-34 44 54	$-0.4 \rightarrow -1$	$186 \pm 4$	9-12	-6.0
Ter 8	19 38 30.3	-34 07 05	$-1.99 \pm 0.08$	$158 \pm 8$	16-19	-5.0
Arp 2	19 25 33.9	-30 27 26	$-1.70 \pm 0.11$	$154 \pm 10$	13-14	-5.3

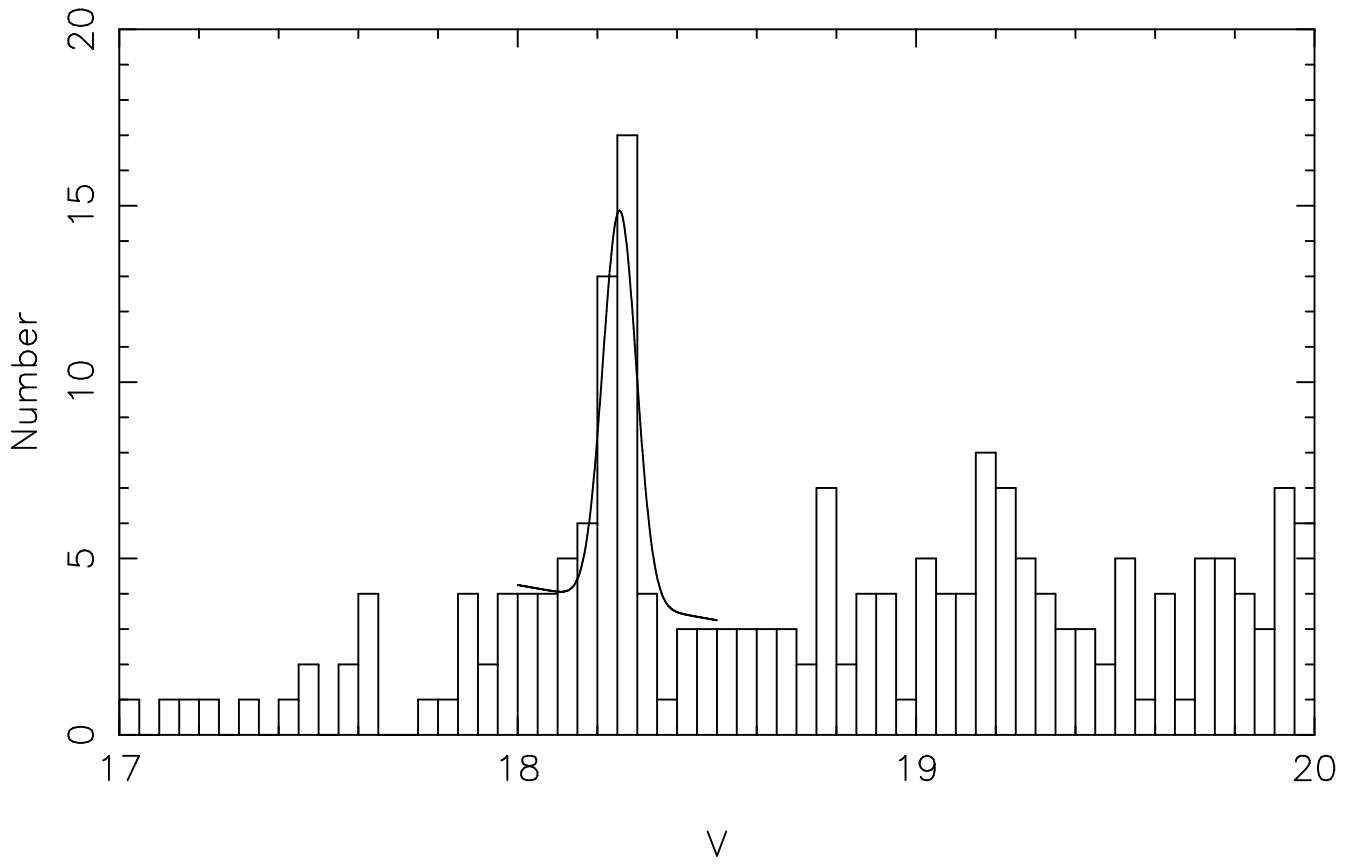




TABLE 2.A. AAT Radial Velocity Data Aug94

ra (1950)	dec (1950)	R mag	$B_J - R$	$V_{helio}$ (km/s)	CTIO?
18 55 25.96	-30 41 46.0	15.30	2.03	125.	y
18 55 02.53	-30 41 57.7	15.09	2.22	133.	y
18 55 00.94	-30 44 12.5	14.86	1.95	114.	n
18 54 24.42	-30 44 23.1	15.28	1.77	129.	y
18 54 17.86	-30 44 45.8	14.77	2.75	136.	y
18 55 33.88	-30 44 49.8	14.95	2.28	143.	y
18 55 53.49	-30 45 14.7	15.18	1.91	128.	y
18 54 49.27	-30 48 46.7	15.20	1.82	139.	y
18 56 13.73	-30 49 45.4	15.18	2.13	149.	y
18 55 47.49	-30 50 06.9	15.40	1.62	157.	y
18 55 19.48	-30 51 44.6	14.99	2.19	163.	n
18 53 57.84	-30 52 14.5	15.39	1.81	137.	y
18 56 13.84	-30 52 31.8	15.31	1.88	142.	y
18 54 23.52	-30 52 34.6	15.28	1.90	138.	y
18 54 38.77	-30 53 00.9	15.22	1.83	145.	y
18 54 56.02	-30 53 56.9	15.22	1.89	-67.	n
18 54 04.32	-30 54 01.2	14.76	2.14	165.	y
18 55 02.63	-30 54 25.0	14.79	2.40	180.	n
18 55 29.92	-30 54 57.5	15.01	2.32	143.	y
18 55 58.45	-30 55 26.2	15.31	1.83	153.	y
18 55 06.99	-30 56 07.8	15.15	1.93	141.	y
18 56 21.41	-30 56 10.1	15.09	2.08	160.	y
18 55 26.47	-30 56 12.7	14.89	2.11	154.	n
18 54 15.26	-30 56 31.7	14.90	2.18	134.	y
18 55 41.70	-30 57 00.9	14.95	2.08	152.	y
18 54 12.85	-30 57 08.7	14.63	2.05	153.	y
18 55 33.79	-30 57 31.2	14.92	2.12	129.	y
18 53 46.48	-30 58 45.2	15.00	1.91	123.	y
18 54 03.43	-30 59 12.2	15.15	2.17	147.	y
18 55 01.84	-30 59 16.2	14.75	3.20	153.	y
18 55 48.56	-31 00 28.5	14.32	1.56	157.	y
18 54 18.10	-31 00 39.3	14.79	2.16	153.	y
18 56 25.41	-31 01 25.3	14.45	2.31	151.	y
18 54 29.75	-31 01 56.5	14.36	1.93	144.	y
18 55 24.63	-31 02 01.6	15.29	1.95	-7.	n

TABLE 2.A. (continued)

ra (1950)	dec (1950)	R mag	$B_J - R$	$V_{helio}$ (km/s)	CTIO?
18 55 44.59	-31 03 20.3	14.53	2.38	135.	y
18 55 14.26	-31 03 57.4	14.55	2.16	175.	n
18 54 19.74	-31 05 26.0	15.49	1.78	140.	y
18 55 49.54	-31 08 30.7	14.97	2.05	141.	y
18 54 07.42	-31 08 49.6	14.06	2.31	144.	y
18 54 16.99	-31 08 54.6	14.13	1.71	73.	n
18 55 51.17	-31 10 02.9	14.16	1.98	135.	y
18 48 01.69	-31 10 04.1	14.69	2.28	141.	y
18 55 31.26	-31 10 36.7	15.06	2.03	150.	y
18 54 48.93	-31 10 37.3	14.41	1.68	138.	y
18 55 26.58	-31 10 42.8	14.99	2.47	137.	y
18 53 46.67	-31 10 45.2	14.47	1.87	134.	y
18 47 45.26	-31 10 48.5	15.02	1.92	133.	y
18 54 22.38	-31 11 00.8	15.22	2.10	135.	y
18 54 38.63	-31 11 55.7	14.97	2.27	147.	y
18 47 44.02	-31 11 57.7	14.36	2.31	182.	n
18 47 33.76	-31 11 59.5	15.55	1.98	161.	y
18 53 37.93	-31 12 14.1	15.23	2.02	154.	n
18 55 09.59	-31 12 21.1	14.97	2.14	140.	y
18 55 46.52	-31 12 40.0	15.34	1.88	135.	y
18 54 19.55	-31 13 09.6	14.51	1.82	107.	n
18 48 50.90	-31 13 21.5	14.51	2.18	160.	y
18 54 13.88	-31 13 26.1	14.45	2.07	145.	y
18 47 25.30	-31 15 17.6	15.21	1.90	170.	y
18 54 57.98	-31 15 28.1	14.25	2.05	-68.	n
”	”	”	”	-65.	n
18 48 01.66	-31 15 30.4	15.00	2.13	125.	y
18 54 52.05	-31 16 05.7	14.38	2.03	17.	n
18 49 04.92	-31 16 16.6	14.50	1.75	158.	y
18 54 37.41	-31 16 38.1	14.96	2.23	165.	y
”	”	”	”	160.	y
18 54 22.91	-31 16 39.2	15.38	2.13	137.	y
18 48 43.80	-31 16 54.6	15.07	1.99	145.	y
18 54 30.52	-31 16 59.5	15.38	2.13	148.	y
18 48 21.94	-31 17 39.6	14.45	1.95	21.	n

TABLE 2.A. (continued)

ra (1950)	dec (1950)	R mag	$B_J - R$	$V_{helio}$ (km/s)	CTIO?
18 47 18.97	-31 17 48.0	15.15	1.79	-4.	n
18 48 41.16	-31 19 19.2	14.94	2.07	-40.	n
18 48 25.98	-31 20 01.2	15.29	1.81	-38.	n
18 53 51.60	-31 20 33.6	14.09	1.59	164.	n
18 54 05.59	-31 21 31.6	14.82	2.21	138.	n
18 53 50.75	-31 22 26.6	14.93	2.12	-15.	n
18 53 43.32	-31 22 33.0	15.34	1.92	154.	n
18 55 19.91	-31 23 17.1	15.30	2.42	-37.	n
18 54 59.29	-31 23 19.0	14.97	2.12	172.	n
18 55 13.17	-31 23 47.0	14.51	2.28	157.	n
18 47 59.56	-31 23 49.0	14.50	1.89	137.	y
18 47 46.27	-31 23 53.0	15.03	2.33	153.	y
18 49 03.00	-31 23 56.8	14.77	2.06	158.	y
18 47 56.77	-31 23 59.1	15.32	2.02	143.	n
18 53 38.04	-31 24 27.9	15.15	2.33	152.	n
18 48 46.51	-31 24 50.5	15.37	1.97	146.	n
18 48 33.54	-31 24 54.0	14.67	1.81	158.	n
18 54 05.52	-31 25 10.9	15.41	2.27	136.	n
18 53 13.91	-31 25 47.7	15.08	2.19	155.	n
18 46 45.45	-31 26 06.1	14.96	1.90	158.	y
18 47 20.66	-31 27 07.3	14.94	2.28	148.	y
18 53 36.11	-31 27 09.4	14.50	2.11	170.	n
18 53 46.92	-31 27 12.9	14.46	2.09	170.	n
18 48 03.83	-31 27 15.5	15.17	2.11	14.	n
18 48 15.43	-31 27 43.5	15.25	2.05	-25.	n
18 54 39.07	-31 27 43.7	14.98	1.97	156.	n
18 47 47.02	-31 28 13.5	14.32	1.55	-5.	n
18 54 39.56	-31 28 23.6	15.36	2.00	149.	n
18 47 59.55	-31 29 10.9	15.45	2.04	165.	y
18 54 10.02	-31 29 14.5	15.18	1.97	145.	n
18 47 00.40	-31 29 16.2	14.34	1.84	130.	y
18 49 20.68	-31 29 17.8	14.94	1.95	141.	y
18 55 32.46	-31 29 22.5	15.32	2.14	161.	n
18 47 37.48	-31 29 28.5	14.19	1.72	128.	y
18 49 21.78	-31 29 48.6	15.22	2.01	158.	n

TABLE 2.A. (continued)

ra (1950)	dec (1950)	R mag	$B_J - R$	$V_{helio}$ (km/s)	CTIO?
18 55 22.10	-31 29 50.5	15.37	2.07	129.	n
18 55 17.77	-31 30 11.8	15.43	1.94	-43.	n
18 53 02.59	-31 30 27.4	15.45	1.86	172.	n
18 49 20.70	-31 31 04.2	15.51	1.98	165.	y
18 54 41.30	-31 33 13.3	15.11	1.97	-1.	n
18 48 14.44	-31 34 11.2	15.41	2.08	-3.	n
18 49 27.94	-31 34 23.0	14.61	2.32	126.	n
18 48 28.38	-31 34 55.1	14.95	1.85	105.	n
18 47 27.55	-31 35 13.2	15.00	2.06	144.	y
18 53 19.38	-31 35 38.0	15.44	1.71	134.	n
18 53 44.03	-31 35 56.1	14.38	1.81	136.	n
18 48 55.51	-31 36 04.8	14.74	2.26	147.	y
18 48 33.66	-31 36 15.3	14.61	2.15	166.	y
18 54 14.60	-31 36 27.6	14.42	1.91	151.	n
18 55 15.55	-31 37 01.8	15.35	1.99	127.	n
18 47 43.30	-31 37 36.5	14.71	2.03	147.	y
18 47 19.00	-31 38 24.6	15.04	2.02	149.	y
18 54 10.42	-31 39 09.9	14.99	2.05	147.	n
18 53 48.90	-31 39 14.4	14.52	2.19	153.	n
18 47 57.16	-31 39 47.4	15.33	1.92	136.	y
18 47 32.69	-31 40 15.8	14.81	2.03	-9.	n
19 15 26.75	-32 26 46.2	15.46	2.08	1.	n
19 20 44.30	-32 30 17.1	15.07	2.30	170.	n
19 15 41.02	-32 30 53.7	15.19	2.14	135.	n
19 16 06.94	-32 32 00.3	15.29	2.06	138.	n
19 21 14.29	-32 32 58.0	15.54	2.11	139.	n
19 15 12.19	-32 34 09.0	13.08	2.24	13.	n
19 20 02.82	-32 34 29.3	14.91	2.28	140.	n
19 20 44.34	-32 36 56.3	15.29	2.20	129.	n
19 21 44.99	-32 37 44.3	15.14	1.93	137.	n
19 21 21.70	-32 37 56.3	14.96	2.05	157.	n
19 16 03.67	-32 38 31.3	15.69	2.25	-5.	n
19 21 39.69	-32 40 04.9	15.14	2.18	40.	n
19 20 53.36	-32 40 45.5	15.56	2.36	13.	n
19 21 06.08	-32 41 10.7	15.37	1.97	94.	n

TABLE 2.A. (continued)

ra (1950)	dec (1950)	R mag	$B_J - R$	$V_{helio}$ (km/s)	CTIO?
19 21 20.45	-32 41 48.9	14.44	2.41	154.	n
19 13 52.32	-32 42 09.1	15.20	2.27	166.	n
19 19 35.20	-32 42 15.1	15.36	2.27	42.	n
19 21 00.24	-32 42 18.1	15.08	2.01	128.	n
19 21 10.09	-32 42 24.3	15.23	2.28	-21.	n
19 20 29.37	-32 43 22.7	15.61	2.28	127.	n
19 15 58.86	-32 44 29.5	15.62	2.11	-3.	n
19 15 15.71	-32 44 55.6	15.81	2.25	141.	n
19 14 53.63	-32 44 57.4	14.76	2.31	142.	n
19 21 17.54	-32 47 16.3	15.39	2.21	116.	n
19 20 18.77	-32 47 45.4	15.68	2.26	-29.	n
19 16 10.65	-32 48 46.7	15.77	2.32	-41.	n
19 19 41.80	-32 48 54.9	15.05	2.21	131.	n
19 15 06.84	-32 50 10.3	15.08	2.13	-11.	n
19 13 39.66	-32 50 27.0	15.09	2.40	161.	n
19 14 50.27	-32 50 30.8	14.71	2.16	167.	n
19 15 01.27	-32 50 37.7	15.63	2.43	37.	n
19 20 01.88	-32 50 58.5	14.91	2.05	156.	n
19 19 38.98	-32 54 34.0	14.87	2.60	155.	n
19 14 25.80	-32 55 14.5	14.82	2.95	145.	n
19 20 32.64	-32 55 33.2	15.55	2.23	4.	n
19 19 46.17	-32 56 32.3	14.91	2.01	-33.	n
19 20 18.47	-32 57 10.6	14.74	2.65	137.	n
19 14 09.70	-32 57 37.1	15.46	2.23	-10.	n
19 21 22.38	-32 57 42.7	14.61	2.54	128.	n
19 20 44.50	-32 57 55.4	15.53	2.10	-7.	n
19 21 34.91	-32 58 41.7	13.89	2.66	137.	n
19 15 24.17	-32 59 15.5	15.44	2.30	75.	n
19 14 38.09	-33 00 47.3	15.40	2.35	141.	n
19 14 50.33	-33 00 52.3	14.83	2.40	139.	n
19 21 03.00	-33 03 09.3	15.02	2.05	-10.	n
19 20 36.72	-33 03 38.6	14.85	2.36	142.	n
19 38 05.63	-33 17 49.6	15.17	1.79	126.	y
19 37 33.09	-33 21 22.9	14.73	1.86	122.	y
19 38 44.02	-33 22 16.5	15.19	1.67	27.	y

TABLE 2.A. (continued)

ra (1950)	dec (1950)	R mag	$B_J - R$	$V_{helio}$ (km/s)	CTIO?
19 39 40.77	-33 23 03.5	14.15	2.20	130.	y
19 37 57.15	-33 24 21.9	15.25	1.72	122.	y
19 38 52.39	-33 29 23.6	14.85	1.63	-9.	y
19 38 42.52	-33 32 12.8	15.30	1.83	116.	y
19 38 29.04	-33 39 43.6	14.86	1.79	7.	y
19 39 36.86	-33 41 41.7	13.82	3.70	136.	n
19 39 02.82	-33 42 45.1	15.03	1.88	10.	y
19 38 49.57	-33 44 17.7	14.78	1.64	125.	y
19 38 20.91	-33 46 18.1	15.20	1.69	-42.	n
19 38 08.85	-33 46 29.1	15.16	1.87	46.	n
19 38 29.47	-33 48 27.9	15.20	1.83	-34.	n
19 40 08.00	-33 51 29.6	15.23	1.94	-2.	n
19 41 10.80	-33 59 28.2	14.10	2.13	133.	n
19 39 44.91	-34 00 15.8	15.05	1.82	46.	n
19 41 51.21	-34 00 59.5	14.62	1.61	-7.	n
19 20 16.37	-34 03 01.0	14.88	2.28	-10.	n
19 21 00.58	-34 04 21.5	15.10	1.98	33.	n
19 39 55.45	-34 04 35.9	15.48	1.66	129.	n
19 41 08.69	-34 05 03.6	15.03	2.01	-15.	n
19 21 42.27	-34 05 42.8	15.56	2.17	143.	n
19 20 57.62	-34 07 09.0	15.24	2.25	-7.	n
19 20 02.92	-34 07 33.0	15.71	2.23	-42.	n
19 40 55.82	-34 07 48.2	14.70	1.79	129.	n
19 21 56.90	-34 07 53.7	15.14	1.96	-55.	n
19 39 54.45	-34 07 55.1	15.40	1.70	122.	n
19 21 43.27	-34 09 02.4	14.84	2.23	150.	n
19 39 36.10	-34 09 08.4	15.30	1.68	-81.	n
19 41 42.34	-34 10 00.6	15.34	1.69	117.	n
19 19 39.67	-34 10 27.0	14.84	2.41	120.	n
19 22 15.35	-34 10 35.3	15.82	2.23	35.	n
19 41 21.73	-34 12 08.2	15.45	1.75	27.	n
19 21 47.20	-34 12 33.7	14.83	2.43	152.	n
19 35 28.52	-34 14 30.9	15.15	1.74	13.	n
19 19 33.84	-34 17 03.6	14.80	2.11	159.	n
19 20 52.55	-34 18 57.5	14.91	2.04	21.	n

TABLE 2.A. (continued)

ra (1950)	dec (1950)	R mag	$B_J - R$	$V_{helio}$ (km/s)	CTIO?
19 22 04.85	-34 19 29.5	15.43	2.05	18.	n
19 22 32.91	-34 19 43.4	14.99	2.13	-61.	n
19 21 10.45	-34 20 30.5	15.89	2.27	80.	n
19 21 27.34	-34 21 00.9	15.87	2.26	-29.	n
19 19 42.81	-34 21 55.8	15.64	2.31	-6.	n
19 35 25.24	-34 22 16.6	14.65	2.07	149.	y
19 21 07.58	-34 22 24.1	15.04	2.30	40.	n
19 34 39.38	-34 23 49.7	15.10	1.72	44.	n
19 36 17.12	-34 24 33.7	14.93	1.61	133.	y
19 22 08.48	-34 25 26.6	15.19	2.55	-68.	n
19 21 58.41	-34 25 52.6	15.77	2.31	141.	n
19 20 48.79	-34 26 06.3	15.32	2.01	133.	n
19 21 56.75	-34 26 42.5	15.64	2.17	143.	n
19 35 50.75	-34 26 56.7	15.32	1.67	-16.	y
19 20 36.53	-34 29 38.8	15.55	2.25	138.	n
19 36 57.98	-34 29 56.8	15.05	1.90	-23.	y
19 36 17.39	-34 34 05.6	14.68	1.99	0.	y
19 35 49.78	-34 34 07.4	14.65	1.84	9.	y
19 36 08.24	-34 38 05.1	15.18	1.78	-16.	n
19 36 27.42	-34 41 55.7	15.29	2.25	-20.	y
19 35 36.84	-34 46 15.7	14.88	1.75	120.	n

TABLE 2.B. CTIO Radial Velocity Data Aug94

ra (1950)	dec (1950)	R mag	$B_J - R$	$V_{helio}$ (km/s)	$R$	$\Delta V$	AAT?
18 48 49.41	-29 57 52.5	15.05	1.96	124.	6.42	...	n
18 49 16.05	-29 58 01.8	15.83	1.65	159.	6.55	4.74	n
18 49 04.76	-29 58 16.6	15.53	1.77	27.	11.16	...	n
18 48 51.37	-29 58 47.3	15.90	1.60	140.	6.79	5.81	n
18 49 06.06	-29 59 10.9	15.07	1.87	154.	7.27	1.89	n
18 50 29.20	-29 59 12.2	15.35	1.67	122.	10.84	...	n
18 49 54.44	-29 59 39.9	14.67	2.02	134.	7.68	3.06	n
18 50 28.85	-29 59 40.9	15.84	1.62	30.	2.73	47.	n
18 48 51.14	-30 00 20.4	15.56	1.54	-16.	5.07	...	n
18 50 05.13	-30 00 50.1	15.25	1.86	146.	12.28	2.86	n
18 49 20.23	-30 00 56.6	15.73	1.74	4.	8.36	3.4	n
18 50 33.66	-30 01 03.8	15.12	1.84	147.	6.91	7.92	n
18 49 34.70	-30 01 07.7	15.58	1.87	131.	8.14	...	n
18 50 37.79	-30 01 09.0	15.66	1.76	123.	7.68	2.73	n
18 48 48.56	-30 01 14.5	15.92	1.65	151.	6.97	...	n
18 50 47.73	-30 01 19.9	15.64	1.55	115.	2.50	...	n
18 49 05.08	-30 01 26.1	15.12	2.17	147.	8.10	...	n
18 50 47.18	-30 02 22.0	15.21	1.62	147.	10.93	1.09	n
18 49 58.01	-30 02 38.4	15.74	1.62	132.	11.27	...	n
18 50 55.34	-30 02 48.1	15.33	1.70	-53.	8.40	0.25	n
18 49 57.59	-30 03 21.4	14.80	2.04	143.	7.33	2.10	n
18 48 53.50	-30 03 40.5	15.62	1.70	-93.	3.54	...	n
18 49 06.31	-30 04 13.6	15.58	1.80	139.	5.02	213.	n
18 50 16.51	-30 04 21.8	14.57	2.19	113.	9.53	...	n
18 48 31.59	-30 04 24.3	14.82	2.00	19.	9.03	...	n
18 48 33.72	-30 04 46.4	15.69	1.63	150.	3.61	0.53	n
18 49 36.61	-30 04 47.9	15.88	1.82	132.	4.59	43.	n
18 49 26.54	-30 05 10.0	15.49	1.60	-32.	7.70	6.22	n
18 49 35.09	-30 05 11.9	15.55	1.87	82.	10.72	...	n
18 51 00.47	-30 05 23.5	15.53	1.58	141.	8.71	...	n
18 50 27.38	-30 06 20.7	15.18	1.78	153.	11.42	...	n
18 48 11.82	-30 07 27.0	14.76	1.74	-20.	11.10	0.94	n
18 48 59.11	-30 07 35.2	15.32	1.90	145.	6.50	0.51	n
18 50 31.85	-30 07 45.6	15.48	1.81	129.	6.32	5.19	n
18 49 00.75	-30 07 49.9	14.76	1.90	160.	11.36	1.26	n



TABLE 2.B. (continued)

ra (1950)	dec (1950)	R mag	$B_J - R$	$V_{helio}$ (km/s)	$R$	$\Delta V$	AAT?
18 49 56.55	-30 08 14.0	15.64	1.52	141.	3.53	4.97	n
18 51 06.78	-30 08 29.2	15.69	1.53	168.	5.08	11.26	n
18 50 54.22	-30 09 04.4	15.79	1.51	-62.	4.15	183	n
18 51 16.23	-30 09 31.6	15.18	2.00	138.	8.32	...	n
18 49 13.00	-30 09 33.7	15.36	1.55	133.	6.70	2.96	n
18 48 39.12	-30 09 50.5	15.05	1.86	-27.	4.93	14.57	n
18 50 16.72	-30 09 53.7	15.10	2.00	137.	16.77	...	n
18 48 57.93	-30 09 54.0	14.63	1.85	148.	8.46	5.34	n
18 49 20.73	-30 09 54.8	15.71	1.65	-8.	5.05	8.91	n
18 49 38.05	-30 10 03.3	15.54	1.79	147.	9.92	...	n
18 51 16.73	-30 10 14.5	15.55	1.55	138.	4.93	2.14	n
18 50 25.60	-30 10 51.6	15.22	2.15	142.	6.31	4.28	n
18 51 25.16	-30 10 51.8	15.97	1.66	260.	3.42	8.98	n
18 51 25.03	-30 10 58.2	14.69	1.76	145.	4.22	...	n
18 49 39.42	-30 11 23.3	15.17	1.60	154.	14.81	...	n
18 49 27.95	-30 11 27.8	15.28	2.05	139.	12.09	...	n
18 48 34.46	-30 11 28.1	15.50	1.54	-117.	9.31	...	n
18 48 03.81	-30 11 42.4	15.04	1.83	131.	11.82	...	n
18 50 52.78	-30 11 46.9	15.81	1.60	123.	5.27	...	n
18 50 29.41	-30 12 00.1	15.41	1.52	34.	5.89	0.44	n
18 48 31.89	-30 12 01.6	15.28	1.56	17.	7.02	3.20	n
18 50 15.92	-30 12 14.0	15.76	1.63	144.	10.22	2.25	n
18 49 40.30	-30 12 21.4	15.07	2.06	146.	7.44	3.96	n
18 48 10.09	-30 12 26.1	15.71	1.82	-62.	2.88	7.98	n
18 49 56.45	-30 12 34.1	15.00	1.97	131.	7.91	...	n
18 50 16.29	-30 12 52.0	15.53	1.67	141.	11.90	...	n
18 49 15.96	-30 13 02.2	15.90	1.59	115.	7.16	3.87	n
18 48 04.02	-30 13 08.7	15.33	1.84	26.	9.70	0.87	n
18 49 28.43	-30 13 14.5	15.41	1.51	118.	8.82	...	n
18 50 33.23	-30 13 16.3	14.22	1.98	135.	11.51	2.71	n
18 49 42.85	-30 13 17.6	15.97	1.53	-25.	4.71	...	n
18 51 19.00	-30 13 27.0	14.91	2.15	144.	6.34	3.05	n
18 48 41.95	-30 13 27.6	15.90	2.00	-50.	5.17	...	n
18 48 40.10	-30 13 48.3	15.92	1.53	-89.	7.35	...	n
18 51 12.38	-30 13 57.0	15.03	2.01	144.	11.54	...	n

TABLE 2.B. (continued)

ra (1950)	dec (1950)	R mag	$B_J - R$	$V_{helio}$ (km/s)	$R$	$\Delta V$	AAT?
18 49 15.13	-30 14 38.9	14.98	1.81	-74.	8.17	3.57	n
18 50 31.19	-30 15 04.6	15.97	1.71	135.	6.56	...	n
18 48 20.06	-30 15 10.6	15.26	1.85	151.	8.45	1.42	n
18 48 02.15	-30 15 10.8	15.71	1.55	128.	10.11	...	n
18 51 18.03	-30 15 11.5	15.77	2.06	145.	4.48	4.03	n
18 48 13.73	-30 15 11.6	15.18	2.18	147.	5.46	1.30	n
18 50 07.67	-30 15 32.0	14.88	1.96	154.	12.45	...	n
18 48 04.39	-30 15 56.4	15.87	1.55	26.	6.45	2.74	n
18 48 25.92	-30 16 14.3	15.58	1.63	148.	10.47	...	n
18 50 48.88	-30 16 18.3	15.93	1.70	152.	12.67	...	n
18 51 30.38	-30 16 52.9	14.90	1.93	248.	2.34	38.8	n
18 48 06.17	-30 16 56.2	15.82	1.95	26.	8.61	...	n
18 50 27.32	-30 17 18.2	15.75	1.82	-17.	5.10	...	n
18 49 16.40	-30 17 31.9	15.34	1.73	154.	4.99	2.06	n
18 49 15.45	-30 17 50.0	15.55	1.53	45.	4.81	8.31	n
18 49 42.09	-30 17 52.0	15.40	1.73	146.	6.35	2.52	n
18 49 48.30	-30 17 56.1	15.84	1.96	128.	5.92	999.	n
18 50 40.04	-30 18 08.1	15.13	2.20	124.	3.31	2.61	n
18 48 43.72	-30 18 34.6	15.11	2.04	153.	5.75	3.98	n
18 50 49.28	-30 18 36.7	15.89	1.64	135.	6.48	...	n
18 50 10.66	-30 18 40.5	15.04	1.93	-59.	6.71	5.18	n
18 50 58.44	-30 19 14.8	15.11	1.75	-80.	8.70	2.05	n
18 48 23.21	-30 19 33.1	15.71	1.87	159.	11.29	4.23	n
18 50 28.04	-30 19 42.2	14.22	2.15	144.	9.05	...	n
18 48 37.96	-30 20 44.6	15.23	1.84	130.	11.36	...	n
18 50 51.30	-30 20 47.5	15.45	1.59	14.	14.30	...	n
18 50 26.21	-30 20 47.6	15.68	1.83	147.	13.89	...	n
18 51 01.45	-30 21 02.0	15.95	1.52	141.	8.89	...	n
18 49 28.34	-30 21 02.5	15.76	1.58	151.	5.31	9.62	n
18 50 40.63	-30 21 15.8	15.71	1.68	135.	6.13	0.78	n
18 49 15.52	-30 21 15.9	15.97	1.54	10.	8.35	...	n
18 49 37.89	-30 21 19.7	15.00	2.08	130.	8.40	...	n
18 50 36.51	-30 21 20.8	15.14	2.04	129.	3.92	12.46	n
18 49 21.88	-30 21 24.1	15.88	1.74	132.	6.42	0.86	n
18 50 03.78	-30 21 41.6	15.55	1.87	143.	3.68	...	n

TABLE 2.B. (continued)

ra (1950)	dec (1950)	R mag	$B_J - R$	$V_{helio}$ (km/s)	$R$	$\Delta V$	AAT?
18 50 44.09	-30 21 48.5	15.95	1.65	158.	10.12	...	n
18 48 40.83	-30 21 51.1	15.05	1.87	126.	9.31	2.50	n
18 49 05.61	-30 21 58.7	15.49	1.73	151.	4.22	12.4	n
18 50 32.99	-30 22 27.7	15.00	1.67	139.	8.73	4.11	n
18 51 12.78	-30 23 12.6	14.62	1.87	142.	8.01	0.80	n
18 49 40.92	-30 23 18.4	15.59	1.63	-21.	5.67	...	n
18 50 37.07	-30 23 35.4	15.98	1.84	32.	7.82	...	n
18 51 20.34	-30 23 45.2	15.43	1.52	-39.	8.35	1.97	n
18 49 02.28	-30 23 55.7	15.29	1.80	131.	6.71	5.17	n
18 50 43.41	-30 23 56.4	15.88	1.50	5.	5.86	2.10	n
18 48 59.71	-30 24 03.4	15.41	1.86	137.	11.75	...	n
18 48 31.87	-30 24 07.9	15.15	2.11	-47.	4.27	...	n
18 50 29.20	-30 24 26.7	15.47	1.83	132.	7.18	1.22	n
18 50 01.06	-30 25 24.3	15.68	1.86	143.	5.06	5.2	n
18 49 26.23	-30 25 30.0	15.58	1.73	140.	6.82	0.27	n
18 50 17.27	-30 25 36.4	14.59	2.13	145.	7.31	1.75	n
18 49 15.59	-30 26 00.8	14.76	1.84	127.	9.80	0.08	n
18 49 21.30	-30 26 11.9	14.80	1.83	141.	7.56	...	n
18 51 12.04	-30 26 14.7	15.77	1.62	146.	8.94	2.01	n
18 50 55.46	-30 26 24.9	15.62	1.64	142.	10.00	0.44	n
18 51 18.91	-30 26 37.9	14.96	2.08	138.	8.06	6.4	n
18 49 14.54	-30 26 50.9	15.84	1.87	126.	6.90	...	n
18 49 38.05	-30 26 51.0	15.78	1.56	45.	8.45	2.87	n
18 49 21.91	-30 27 23.9	15.78	1.73	148.	9.89	3.13	n
18 48 45.95	-30 27 30.2	15.06	2.02	150.	7.67	2.28	n
18 50 10.31	-30 27 32.1	15.57	1.72	153.	7.22	...	n
18 48 43.64	-30 27 36.3	15.22	1.87	129.	12.17	3.32	n
18 51 20.89	-30 27 46.7	15.97	1.77	132.	8.75	0.93	n
18 49 50.41	-30 27 54.7	15.78	1.69	146.	3.06	3.95	n
18 51 03.58	-30 28 01.3	15.62	1.87	138.	5.60	0.00	n
18 49 40.45	-30 28 15.1	15.08	1.97	136.	4.49	2.06	n
18 49 31.88	-30 28 26.9	15.55	1.61	132.	10.35	1.00	n
18 51 00.27	-30 28 57.4	14.96	1.99	142.	5.90	2.78	n
18 48 55.73	-30 29 00.9	15.28	1.76	156.	6.05	199.	n
18 50 01.49	-30 29 02.1	15.77	1.95	152.	7.94	...	n

TABLE 2.B. (continued)

ra (1950)	dec (1950)	R mag	$B_J - R$	$V_{helio}$ (km/s)	$R$	$\Delta V$	AAT?
18 48 16.00	-30 29 04.7	15.46	1.76	169.	6.61	6.21	n
18 50 38.69	-30 29 07.2	15.86	1.52	7.	3.17	5.37	n
18 48 25.75	-30 29 24.1	15.69	1.71	-50.	2.33	207.	n
18 50 58.38	-30 30 04.2	15.12	1.59	139.	7.60	...	n
18 49 10.63	-30 30 04.7	15.56	1.83	36.	5.73	7.02	n
18 48 34.27	-30 30 06.0	15.43	1.75	155.	6.77	2.53	n
18 50 50.55	-30 30 36.6	14.34	1.93	73.	8.55	3.61	n
18 50 14.34	-30 30 52.7	15.94	1.97	13.	4.15	325	n
18 48 51.73	-30 30 59.7	15.61	1.68	3.	5.19	2.89	n
18 49 14.64	-30 31 34.8	15.55	1.67	111.	12.60	...	n
18 49 36.49	-30 31 35.9	15.34	1.95	163.	9.76	...	n
18 49 02.12	-30 31 47.2	15.08	2.19	131.	8.50	...	n
18 48 55.91	-30 32 03.8	14.88	2.04	2.	10.42	2.61	n
18 49 51.51	-30 32 18.5	15.30	1.80	154.	9.78	...	n
18 48 31.70	-30 32 32.1	15.33	1.73	145.	14.36	...	n
18 48 41.64	-30 32 47.8	15.37	1.51	-51.	7.74	3.4	n
18 50 36.92	-30 33 48.9	15.67	1.64	118.	3.11	6.34	n
18 50 15.29	-30 34 14.4	15.72	1.71	212.	2.44	126.	n
18 50 33.02	-30 34 42.1	15.52	1.91	144.	10.96	...	n
18 50 26.01	-30 34 45.8	15.73	1.88	141.	2.89	209.	n
18 49 00.22	-30 35 14.6	15.97	1.76	149.	2.63	999.	n
18 55 25.96	-30 41 46.0	15.30	2.03	127.	8.06	1.78	y
18 55 02.53	-30 41 57.7	15.09	2.07	145.	7.17	2.01	y
18 54 24.42	-30 44 23.1	15.28	1.77	144.	7.74	4.06	y
18 54 17.86	-30 44 45.8	14.77	3.04	149.	5.96	1.41	y
18 55 33.88	-30 44 49.8	14.95	1.96	141.	12.80	1.32	y
18 55 53.49	-30 45 14.7	15.18	1.79	139.	10.63	2.26	y
18 54 49.27	-30 48 46.7	15.20	1.75	144.	6.06	0.54	y
18 56 13.73	-30 49 45.4	15.18	2.09	147.	6.65	0.36	y
18 55 47.49	-30 50 06.9	15.40	1.62	158.	8.08	0.00	y
18 53 57.84	-30 52 14.5	15.39	1.75	145.	10.32	0.92	y
18 56 13.84	-30 52 31.8	15.31	1.78	134.	10.35	0.21	y
18 54 23.52	-30 52 34.6	15.28	1.82	139.	9.00	3.47	y
18 54 38.77	-30 53 00.9	15.22	1.69	134.	6.84	2.06	y
18 54 04.32	-30 54 01.2	14.76	2.01	162.	10.32	0.98	y

TABLE 2.B. (continued)

ra (1950)	dec (1950)	R mag	$B_J - R$	$V_{helio}$ (km/s)	$R$	$\Delta V$	AAT?
18 55 29.92	-30 54 57.5	15.01	2.20	137.	11.06	3.00	y
18 55 58.45	-30 55 26.2	15.31	1.66	147.	10.31	1.43	y
18 55 06.99	-30 56 07.8	15.15	1.73	140.	11.40	2.15	y
18 56 21.41	-30 56 10.1	15.09	2.01	153.	7.39	7.08	y
18 54 15.26	-30 56 31.7	14.90	2.08	141.	10.46	3.47	y
18 55 41.70	-30 57 00.9	14.95	2.08	148.	9.69	3.46	y
18 54 12.85	-30 57 08.7	14.63	2.05	154.	12.47	0.36	y
18 55 33.79	-30 57 31.2	14.92	2.09	122.	6.47	3.21	y
18 53 46.48	-30 58 45.2	15.00	1.90	122.	7.13	1.13	y
18 54 03.43	-30 59 12.2	15.15	2.06	148.	9.62	0.04	y
18 55 01.84	-30 59 16.2	14.75	3.11	152.	10.63	0.09	y
18 55 48.56	-31 00 28.5	14.32	1.56	154.	15.68	1.42	y
18 54 18.10	-31 00 39.3	14.79	1.88	154.	13.70	0.27	y
18 56 25.41	-31 01 25.3	14.45	2.31	148.	7.59	2.48	y
18 54 29.75	-31 01 56.5	14.36	1.93	141.	13.08	0.01	y
18 55 44.59	-31 03 20.3	14.53	2.64	127.	9.02	3.46	y
18 54 19.74	-31 05 26.0	15.49	1.81	149.	8.14	1.24	y
18 55 49.54	-31 08 30.7	14.97	1.87	142.	8.68	0.66	y
18 54 07.42	-31 08 49.6	14.06	2.17	146.	7.87	0.28	y
18 55 51.17	-31 10 02.9	14.16	1.88	130.	12.99	0.38	y
18 48 01.69	-31 10 04.1	14.69	2.16	136.	8.71	...	y
18 55 31.26	-31 10 36.7	15.06	2.03	139.	6.27	6.28	y
18 54 48.93	-31 10 37.3	14.41	1.68	137.	8.88	0.99	y
18 55 26.58	-31 10 42.8	14.99	2.33	137.	6.60	3.92	y
"	"	"	"	134.	6.24	1.02	y
18 53 46.67	-31 10 45.2	14.47	1.71	133.	9.60	1.38	y
18 47 45.26	-31 10 48.5	15.02	1.84	131.	13.14	...	y
18 54 22.38	-31 11 00.8	15.22	2.02	135.	5.86	0.83	y
18 54 38.63	-31 11 55.7	14.97	2.17	145.	7.66	0.44	y
18 47 33.76	-31 11 59.5	15.55	1.89	163.	4.18	...	y
18 55 09.59	-31 12 21.1	14.97	2.00	137.	10.32	0.44	y
18 55 46.52	-31 12 40.0	15.34	1.80	129.	7.34	6.95	y
18 48 50.90	-31 13 21.5	14.51	2.08	154.	13.39	...	y
18 54 13.88	-31 13 26.1	14.45	1.92	140.	11.15	1.74	y
18 47 25.30	-31 15 17.6	15.21	1.87	165.	12.21	...	y

TABLE 2.B. (continued)

ra (1950)	dec (1950)	R mag	$B_J - R$	$V_{helio}$ (km/s)	$R$	$\Delta V$	AAT?
18 48 01.66	-31 15 30.4	15.00	2.07	119.	12.34	...	y
18 49 04.92	-31 16 16.6	14.50	1.75	151.	12.18	...	y
18 54 37.41	-31 16 38.1	14.96	2.13	157.	7.69	2.19	y
"	"	"	"	155.	10.26	0.75	y
18 54 22.91	-31 16 39.2	15.38	2.04	141.	4.71	6.05	y
18 48 43.80	-31 16 54.6	15.07	1.82	147.	12.10	...	y
18 54 30.52	-31 16 59.5	15.38	2.05	146.	10.09	1.77	y
18 47 59.56	-31 23 49.0	14.50	1.88	127.	12.72	...	y
18 47 46.27	-31 23 53.0	15.03	2.34	146.	15.23	...	y
18 49 03.00	-31 23 56.8	14.77	1.93	154.	12.13	...	y
18 46 45.45	-31 26 06.1	14.96	1.91	149.	13.00	...	y
18 47 20.66	-31 27 07.3	14.94	2.15	142.	12.34	...	y
18 47 59.55	-31 29 10.9	15.45	1.97	158.	10.95	...	y
18 47 00.40	-31 29 16.2	14.34	1.54	117.	16.47	...	y
18 49 20.68	-31 29 17.8	14.94	1.86	141.	14.99	...	y
18 47 37.48	-31 29 28.5	14.19	1.61	122.	7.69	...	y
18 49 20.70	-31 31 04.2	15.51	1.94	156.	13.26	...	y
18 47 27.55	-31 35 13.2	15.00	2.04	138.	11.29	...	y
18 48 55.51	-31 36 04.8	14.74	2.24	149.	12.27	...	y
18 48 33.66	-31 36 15.3	14.61	2.02	158.	12.95	...	y
18 47 43.30	-31 37 36.5	14.71	2.03	143.	10.78	...	y
18 47 19.00	-31 38 24.6	15.04	1.91	147.	10.47	...	y
18 47 57.16	-31 39 47.4	15.33	1.92	137.	8.94	...	y
19 37 49.38	-33 08 27.5	14.54	2.21	128.	5.86	2.07	n
19 38 58.54	-33 11 41.0	14.82	1.80	0.	3.87	7.12	n
19 36 45.44	-33 14 45.5	14.95	1.64	143.	5.61	10.4	n
19 38 47.52	-33 16 15.3	14.23	2.08	-16.	8.04	1.51	n
19 39 23.29	-33 16 26.7	15.43	1.94	125.	6.00	0.16	n
19 38 05.63	-33 17 49.6	15.17	1.79	135.	4.65	6.87	y
19 36 34.68	-33 19 32.7	15.18	1.82	18.	3.93	113.	n
19 37 33.09	-33 21 22.9	14.73	1.86	128.	3.82	155.	y
19 38 44.02	-33 22 16.5	15.19	1.67	35.	5.84	3.36	y
19 39 40.77	-33 23 03.5	14.15	2.20	140.	6.65	6.16	y
19 39 44.91	-33 24 13.1	14.41	1.66	104.	7.71	1.24	n
19 37 57.15	-33 24 21.9	15.25	1.72	131.	6.38	3.14	y

TABLE 2.B. (continued)

ra (1950)	dec (1950)	R mag	B <sub>J</sub> – R	$V_{helio}$ (km/s)	$R$	$\Delta V$	AAT?
19 37 37.89	–33 25 10.6	15.22	1.62	104.	4.42	3.64	n
19 38 52.39	–33 29 23.6	14.85	1.63	–4.	7.02	6.78	y
19 38 42.52	–33 32 12.8	15.30	1.83	124.	4.51	1.84	y
19 36 43.19	–33 33 46.6	14.86	1.63	–33.	6.65	2.22	n
19 38 29.04	–33 39 43.6	14.86	1.79	3.	4.17	151.	y
19 37 32.34	–33 40 35.5	14.14	2.44	130.	6.10	0.06	n
19 39 02.82	–33 42 45.1	15.03	1.88	7.	4.37	143.	y
19 38 49.57	–33 44 17.7	14.78	1.64	241.	2.62	224.	y
19 35 57.83	–34 12 21.6	14.63	1.66	142.	9.55	...	n
19 37 38.70	–34 15 42.8	14.39	1.85	127.	12.85	...	n
19 35 25.24	–34 22 16.6	14.65	2.07	145.	8.96	...	y
19 36 44.88	–34 22 24.2	14.08	1.69	–32.	7.89	...	n
19 37 31.53	–34 22 36.6	15.33	1.68	–68.	7.20	...	n
19 36 17.12	–34 24 33.7	14.93	1.61	140.	6.92	...	y
19 36 25.60	–34 25 01.8	14.32	1.95	81.	12.84	...	n
19 35 50.75	–34 26 56.7	15.32	1.67	–23.	6.89	...	y
19 37 40.20	–34 27 26.0	15.11	1.80	134.	14.09	...	n
19 36 57.98	–34 29 56.8	15.05	1.90	–24.	9.74	...	y
19 38 26.74	–34 31 04.9	15.01	1.74	122.	13.60	...	n
19 38 16.77	–34 33 07.7	15.12	1.75	147.	12.17	...	n
19 36 17.39	–34 34 05.6	14.68	1.99	–0.	7.35	...	y
19 35 49.78	–34 34 07.4	14.65	1.84	6.	6.92	...	y
19 37 45.49	–34 36 30.9	15.47	1.62	–180.	6.90	...	n
19 37 54.05	–34 38 04.1	15.27	1.82	131.	12.67	...	n
19 36 53.26	–34 40 07.1	14.04	1.65	–195.	12.21	...	n
19 36 27.42	–34 41 55.7	15.29	2.25	–23.	3.41	...	y
19 37 35.03	–34 43 32.8	14.75	1.87	146.	11.64	...	n

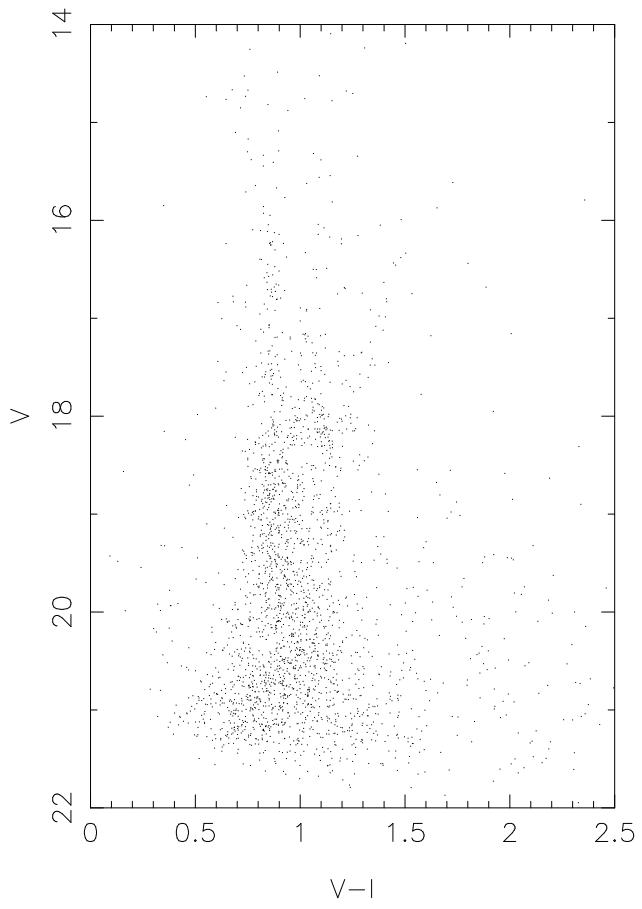




TABLE 3. Mean velocities and dispersions (in km/s) in the observed Sgr fields

Field	Instr.	$\ell$	$b$	$\langle v_{Gal} \rangle$	$\delta v_{Gal}$	$\sigma_v$	$\delta\sigma_v$	No. of stars
f7	CTIO	5.675	-13.588	170.990	0.799	11.414	0.734	114
f6	CTIO	4.442	-13.700	169.530	2.763	13.290	1.538	24
f5	CTIO	5.446	-14.895	171.510	1.222	9.243	1.042	48
f1	CTIO	5.976	-24.345	159.577	2.063	10.800	1.932	20
f7	AAT	5.795	-13.589	169.047	2.318	16.007	1.621	44
f5	AAT	4.444	-13.732	172.154	2.237	14.697	2.122	30
f3	AAT	5.859	-20.624	168.952	2.463	13.663	2.185	17
f1	AAT	6.007	-24.544	155.447	2.368	7.977	1.602	15
f8	AAT	4.859	-11.881	167.840	3.302	18.695	1.799	33
f6	AAT	4.444	-13.732	172.154	2.332	14.697	1.758	30
f4	AAT	5.035	-19.410	172.548	1.924	11.956	1.579	26
f2	AAT	4.330	-21.204	165.293	3.184	11.025	1.810	9

